

DRAFT VERSION FEBRUARY 1, 2023
 Typeset using **LATEX preprint2** style in AASTeX63

LOTUS: A (non-)LTE Optimization Tool for Uniform derivation of Stellar atmospheric parameters

YANGYANG LI(李扬洋)  ¹ AND RANA EZZEDDINE  ^{1, 2}

¹Department of Astronomy, University of Florida, Bryant Space Science Center, Gainesville, FL 32611, USA

²Joint Institute for Nuclear Astrophysics - Center for Evolution of the Elements, USA

(Received August 23, 2022; Revised January 09, 2023; Accepted January 27, 2023)

Submitted to AJ

ABSTRACT

Precise fundamental atmospheric stellar parameters and abundance determination of individual elements in stars are important for all stellar population studies. Non-Local Thermodynamic Equilibrium (Non-LTE; hereafter NLTE) models are often important for such high precision, however, can be computationally complex and expensive, which renders the models less utilized in spectroscopic analyses. To alleviate the computational burden of such models, we developed a robust 1D, NLTE fundamental atmospheric stellar parameter derivation tool, LOTUS, to determine the effective temperature T_{eff} , surface gravity $\log g$, metallicity [Fe/H] and microturbulent velocity v_{mic} for FGK type stars, from equivalent width (EW) measurements of Fe I and Fe II lines. We utilize a generalized curve of growth method to take into account the EW dependencies of each Fe I and Fe II line on the corresponding atmospheric stellar parameters. A global differential evolution optimization algorithm is then used to derive the fundamental parameters. Additionally, LOTUS can determine precise uncertainties for each stellar parameter using a Markov Chain Monte Carlo (MCMC) algorithm. We test and apply LOTUS on a sample of benchmark stars, as well as stars with available asteroseismic surface gravities from the K2 survey, and metal-poor stars from the *Gaia*-ESO and *R*-process Alliance (RPA) surveys. We find very good agreement between our NLTE-derived parameters in LOTUS to non-spectroscopic values on average within $T_{\text{eff}} = \pm 30$ K and $\log g = \pm 0.10$ dex for benchmark stars. We provide open access of our code, as well as of the interpolated pre-computed NLTE EW grids available on Github  ^{a)}, and documentation with working examples on Readthedocs .

Keywords: Astronomical techniques (1684), Spectroscopy (1558); Stellar atmospheres (1584), Stellar physics (1621), Stellar photospheres (1237); Fundamental

Corresponding author: Yangyang Li
 yangyangli@ufl.edu

^{a)} The software is available on GitHub <https://github.com/Li-Yangyang/LOTUS> under a MIT License and version 0.1.1 (as the persistent version) is archived in Zenodo (Li & Ezzeddine 2023).

parameters of stars (555), Astrometry (80), Effective temperature (449), Surface gravity (1669), Metallicity (1031)

1. INTRODUCTION

Precise characterization of stellar spectra is a key ingredient for understanding several fields of modern astrophysics, including the physical and chemical properties and abundances of stars (Asplund et al. 2009; Jofré et al. 2019), galactic formation and evolution (Audouze & Tinsley 1976; McWilliam 1997; Kobayashi et al. 2006), as well as macro and micro physical phenomena near the surface of stars (Miesch & Toomre 2009; Linsky 2017). This accurate level of characterization is also needed for the detection of extra-solar planets when using radial velocity methods (Vanderburg et al. 2016).

With the current inflow of stellar spectra from ongoing and future large observational spectroscopic surveys including, SDSS-V (Kollmeier et al. 2017, R~2000 and ~22500), LAMOST (Liu et al. 2020, R~7500; Cui et al. 2012; Zhao et al. 2012; Deng et al. 2012, R~1800), APOGEE (Ahumada et al. 2020, R~22500), RAVE (Steinmetz et al. 2020, R~7500), GALAH (De Silva et al. 2015, R~28000), as well as the upcoming WEAVE (Dalton et al. 2016, R~5000 and R~20000), 4MOST (de Jong et al. 2019, R~20000) and PLATO (Miglio et al. 2017), stellar spectroscopy will be providing $\sim 10^5$ of golden opportunities to study the chemical and dynamical properties of stars in the Galaxy to help understand its build-up history and evolution.

Atmospheric fundamental stellar parameters, including the effective temperature T_{eff} , surface gravity $\log g$, metallicity [Fe/H] and microturbulent velocity v_{mic} , as well as chemical abundances of stars, are determined from the observed spectra of a given star by fitting theoretical synthetic spectra based on assumptions of geometric structures (1D versus 3D), radiative transfer assumptions (Local Thermody-

namic Equilibrium; hereafter LTE, versus Non-Local Thermodynamic Equilibrium; hereafter NLTE). Two classical methods are commonly used to derive stellar atmospheric parameters from stellar spectra: either 1) by iteratively fitting the observed spectra to synthetic spectral models until a best-fit match is met at the corresponding stellar parameters, or 2) by measuring chemical abundances determined from Fe I and Fe II lines from equivalent widths (EW) measurements, and employing optimization of excitation and ionization equilibrium by changing the stellar parameters iteratively until trends with excitation potential energies (χ) and reduced equivalent widths ($\log(EW/\lambda)$) of the lines are minimized. While the former method of spectral synthesis might outperform the latter in crowded spectral regions or spectra dominated by strong lines ($\log(EW/\lambda) > -4.5$), the EW method generally requires less calculation time and resources than synthetic spectra, making it a simpler and more widely applied tool to measure atmospheric stellar parameters and chemical abundances.

Classical radiative transfer models for deriving stellar parameters and chemical abundances from observed spectra most often LTE. Under LTE, the gas and chemical particles throughout the stellar atmosphere satisfy the Saha-Boltzmann excitation and ionization balance equations. Several stellar atmospheric parameter tools implementing classical 1D and LTE approximations for spectroscopic analyses already exist and are widely used (e.g., MATISSE (Recio-Blanco et al. 2006), MyGIxFOS (Sborodone et al. 2014), the APOGEE pipeline AS-CAP (García Pérez et al. 2016), GALA (Mucciarelli et al. 2013), DOOp (Cantat-Gaudin et al. 2014), ARES (Sousa et al. 2015), StePar (Tabernero et al. 2019), FASMA (Tsantaki &

Andreasen 2021) and iSpec (Blanco-Cuaresma et al. 2014; Blanco-Cuaresma 2019).

The LTE assumption utilized by all of these tools is, however, not physically motivated when applied to evolved giants and/or metal-poor stars (Lind et al. 2012; Ezzeddine et al. 2017; Mashonkina et al. 2017; Amarsi et al. 2020). Inelastic collisional interactions between atoms and electrons or neutral hydrogen in the atmospheres of cool stars usually drive the local conditions in these atmospheres towards LTE. In metal-poor and giant stars, limited electron donors from metals are not able to induce enough collisions to maintain collisional equilibrium in the line-forming regions (Hubeny & Mihalas 2014), which drive line formation away from LTE (Mihalas & Athay 1973; Bergemann et al. 2012). Quantified deviations in abundances and stellar atmospheric parameters from LTE are commonly known as NLTE effects (Asplund 2005), which are mainly driven by deviations from statistical equilibrium or kinematic equilibrium.

A small number of radiative transfer codes have started taking NLTE effects into account for the determination of chemical abundances, including PySME (Wehrhahn 2021), which is based on the spectroscopic analysis code Spectroscopy Made Easy (SME; Piskunov & Valenti 2017). Kovalev et al. (2019) has implemented NLTE departure coefficients in the synthesis tools, allowing NLTE spectral synthesis for certain corresponding absorption lines. More recently, a NLTE version of Turbospectrum (Plez 2012) has been released (Gerber et al. 2022), which also has NLTE departure coefficients incorporated in their 1D, LTE spectral synthesis models. However, both codes allow NLTE corrections for only some elements via spectral synthesis, and stellar parameters still need to be derived independently or iteratively via full spectral fitting, which can be prone to degeneracies. Therefore, a tool that can automatically derive

stellar parameters incorporating NLTE models, taking into account stellar parameter dependences, is highly needed which is the main motivation of this work and paper.

In this work, we present a fast, automatic and robust spectroscopic analysis tool, **LOTUS**, which stands for a “(non-)LTE Optimization Tool for Uniform derivation of Stellar atmospheric parameters”. **LOTUS** allows the derivation of T_{eff} , $\log g$, [Fe/H] and v_{mic} based on EW measurements input of Fe I and Fe II lines from stellar spectra. Either or both LTE and NLTE modes can be chosen for the benefit of comparisons. As compared to traditional full NLTE calculations for each model, **LOTUS** can significantly shorten the time of the determination of stellar parameters using the NLTE assumption from several hours or even days (Hauschildt et al. 1997) to $\sim 15 - 30$ mins for each star. A Monte-Carlo Markov Chain (MCMC) analysis is also implemented to precisely estimate the uncertainties of the derived parameters. We test and apply **LOTUS** on several benchmark stars, and stellar surveys with available non-spectroscopic atmospheric parameters (from asteroseismology or interferometry) for comparison and validation of our results.

The rest of the paper is organized as follows: In Section 2, we present a detailed description of **LOTUS**, and describe the input models for our NLTE calculations, as well as a description of the different modules of the code. In Section 3, we test our code and apply it to derive and compare the derived parameters of benchmark stars, and stars with non-spectroscopic derived parameters. In Section 4, we apply the code to a large sample of metal-poor stars and discuss the NLTE effects obtained via **LOTUS**. In Section 5, we present a discussion on the caveats and limitations of the code, and finally, in Section 6 we present a summary of our results and conclude.

2. GENERAL DESCRIPTION

LOTUS is designed to derive the fundamental atmospheric stellar parameters T_{eff} , $\log g$, [Fe/H] and v_{mic} of FGK type stars, by implementing observed measurements of EW for Fe I and Fe II lines as input. An example of a user input EW linelist is shown in Listing 1 below. The transition wavelength (`obs_wavelength` in Å), element and ionization stage (Fe I or Fe II), measured EW (`obs_ew` in mÅ) and excitation potential energy EP (`obs_ep` in eV) are required.

```

1 obs_wavelength,element,obs_ew,obs_ep
2 4787.8266,FeI,44.2,3.00
3 4788.7566,FeI,65.5,3.24
4 4789.6508,FeI,83.3,3.55
5 6456.3796,FeII,59.2,3.9
6 ...

```

Listing 1. Example of an input file format of observed EW measurements for Fe I and Fe II lines provided by users for LOTUS. `obs_wavelength` are in Å, `obs_ew` in mÅ, and `obs_ep` in eV.

LOTUS has three general modules of functionality. In a general overview, (i) Fe I and Fe II abundances are derived by interpolating a generalized curve of growth (GCOG) for each line in a pre-computed grid of theoretical EW in both LTE and NLTE, following Boeche & Grebel (2016). (ii) the stellar parameters are then derived by minimizing the slopes for excitation and ionization equilibrium, iteratively using a global minimization module, and finally, (iii) uncertainties of the derived atmospheric parameters are estimated utilizing a Markov Chain Monte Carlo (MCMC) algorithm. We describe each of these modules in detail in subsection 2.2 below, after listing the input and radiative transfer models used in Section 2.1.

2.1. Input Models

2.1.1. Stellar Atmosphere Models

LOTUS incorporates 1D, LTE MARCS stellar atmospheric models (Gustafsson et al. 1975, 2008), covering a wide range of stellar parameters typical for FGK stars.

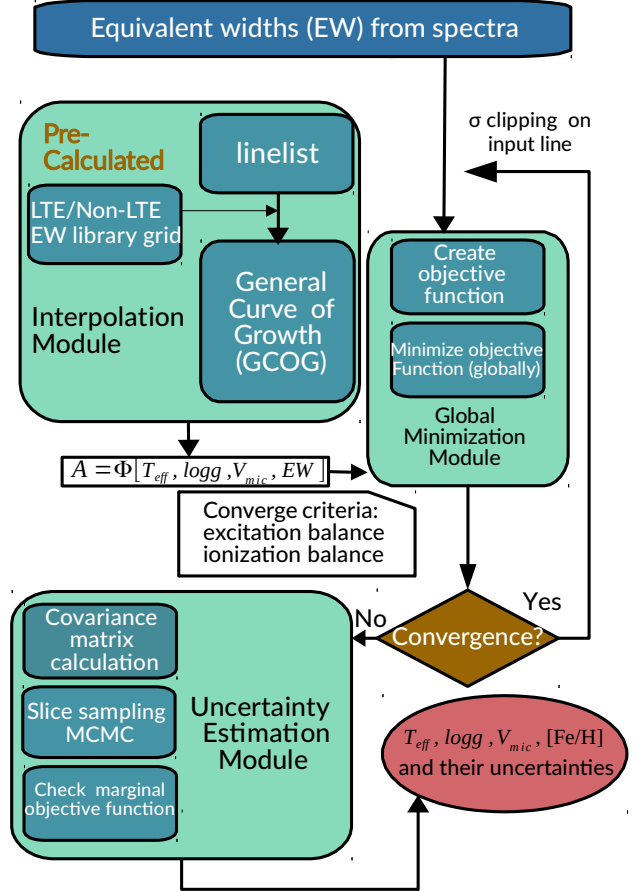


Figure 1. A flow diagram describing the working modules of LOTUS. Three main modules are used to derive the stellar parameters and their uncertainties: (i) an interpolation Module, (ii) a Global Minimization Module, and (iii) an Uncertainty Estimation Module. Input includes EW measurements of Fe I and Fe II of the absorption lines measured in the spectra. Users can define the number of σ clipping required to remove outliers (see Section 2.4.3 for details). Additionally, a halt condition for the value of the smallest allowable minimization function threshold can also be defined by users (see Section 2.4.3 for details).

Spherical atmospheric models were used for $\log g < 3.5$, otherwise, plane-parallel models were adopted. The grid of MARCS model atmosphere available online¹ offers reasonable coverage for the stellar parameters, however

¹ <https://marcs.astro.uu.se/>

they exhibit wide gaps in effective temperature (steps of ~ 250 K), surface gravity (steps of ~ 0.5 cgs), and metallicity (steps of $\sim 0.25 - 0.50$ dex) to optimally explore the parameter space. We utilize the MARCS interpolation subroutine `interp1_marcs.f`² written by Thomas Masseron, to produce a higher resolution grid, with our final parameter grid ranging from 4000 K to 6850 K for T_{eff} (steps of 50 K), $\log g$ from 0.0 to 5.0 (steps of 0.1), [Fe/H] from -3.5 to $+0.5$ (steps of 0.5) and v_{mic} from 0.5 to 3.0 km s^{-1} (steps of 0.5 km s^{-1}).

2.1.2. Iron Model Atom

Computing theoretical NLTE Fe I and Fe II EWs requires the input of a comprehensive iron model with up-to-date radiative and collisional atomic data. For our EW grid calculations, we adopt a well-tested Fe I/Fe II model atom containing 846 Fe I and 1027 Fe II lines Ezzeddine et al. (2016, 2017, 2020). The atom includes absorption line transitions spanning the near-UV to the near-IR, extending the range of wavelength from ~ 1000 to 10^5 \AA . The model also carefully considers hydrogen collision and electron collision processes from quantum atomic data, particularly implementing ion-pair production and mutual-neutralization processes from Barklem (2018). Extensive details on the build-up of the atom and the corresponding atomic data are presented in Ezzeddine et al. (2016) and Ezzeddine et al. (2020).

2.1.3. NLTE Radiative Transfer computations

We utilized the NLTE radiative transfer code `MULTI2.3` to solve for statistical equilibrium populations and derive the theoretical NLTE EW for the Fe I and Fe II lines in our atom. The code utilizes the Approximate Lambda Iteration (ALI) (Rybicki & Hummer 1991) to iteratively determine the populations using the

comprehensive Fe I/Fe II model atom described in Section 2.1.2. `MULTI2.3` also solves for LTE populations using the classical Saha and Boltzmann equations, which is output as a departure coefficient, b_i , where $b_i = n_i(\text{NLTE})/n_i(\text{LTE})$ (Wijbenga & Zwaan 1972), where n is the level population for the corresponding line transition i .

2.1.4. Linelist Selection

The linelist selection is crucial for the accurate derivation of Fe I and Fe II chemical abundances and stellar parameters using the EW method, especially for cooler stars (e.g. FGK stars) since they have much denser spectral line regions containing blended lines. Therefore, we choose a comprehensive list of Fe I and Fe II from the *Gaia*-ESO line list (Jofré et al. 2014; Heiter et al. 2015, 2021), covering the wavelength ranges from 4750 to 6850 \AA and from 8500 to 8950 \AA . Additional lines from the R-Process Alliance (RPA) survey (e.g., Hansen et al. 2018; Sakari et al. 2018; Ezzeddine et al. 2020; Holmbeck et al. 2020) have also been added to account for lines common in metal-poor stars, with corresponding atomic data and references in (Roederer et al. 2018). We combine iron lines from both linelists, removing any duplicates in the process. Our final linelist is presented in Table 2. Future `LOTUS` releases should be easily able to extend the linelists to bluer and redder lines in the UV and IR, respectively.

2.2. Key Modules

Below we describe in detail the key components and modules of the `LOTUS` functionalities. An illustrated flow diagram of the workings of the code is also shown in Figure 1, demonstrating the connection between the different modules.

2.2.1. EW Interpolation Module

² <http://marcs.astro.uu.se/software.php>

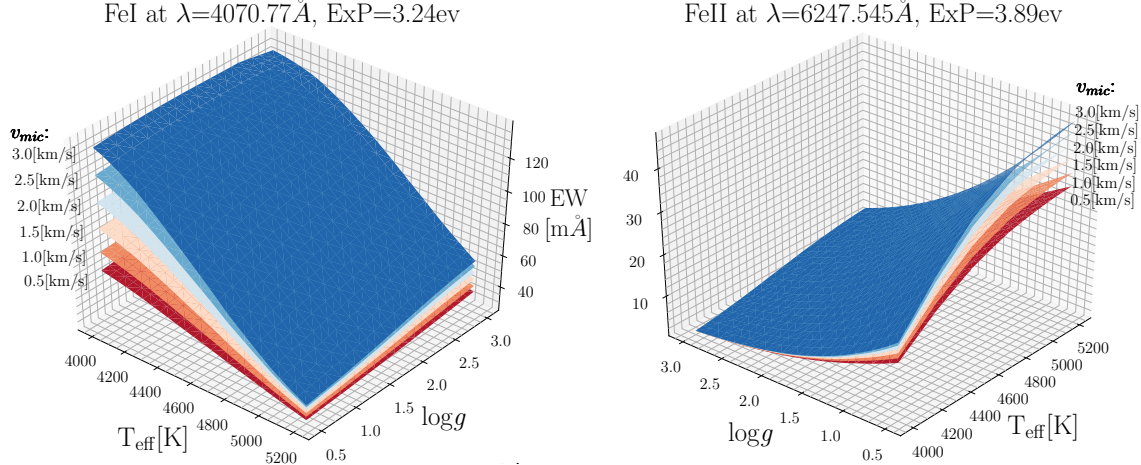


Figure 2. Computed NLTE EW dependence as a function of T_{eff} , $\log g$, v_{mic} for the Fe I line at 4070.77\AA and EP=3.24 eV (left) and the Fe II line at 6247.55\AA with EP=3.89 eV (right). Both lines have been computed at a fixed $[\text{Fe}/\text{H}] = -2.0$.

Traditional curve of growth (COG) methods to derive chemical abundances usually employ simplistic models, typically computed at fixed T_{eff} , $\log g$, $[\text{Fe}/\text{H}]$ and v_{mic} for each line. For some lines, however, EW can have strong dependencies on multiple atmospheric stellar parameters in a given parameter space. Figure 2 demonstrate these dependencies, where EW variation from our computed NLTE grid are shown as a function of T_{eff} , $\log g$ and v_{mic} for the Fe I line at 4070.768\AA (left panel), and the Fe II lines at 6247.545\AA (right panel), respectively. The metallicity for both plots has been fixed at $[\text{Fe}/\text{H}] = -2.00$ for demonstration purposes. We observe that at a fixed $[\text{Fe}/\text{H}]$, increasing T_{eff} will decrease EW of the Fe I line, while EW being mostly insensitive to $\log g$ variation; For Fe II lines, however, increasing T_{eff} will increase EW while increasing $\log g$ will decrease EW. For both lines, EW will increase as v_{mic} increases, as v_{mic} delays the saturation by spreading absorption into a wider wavelength band. These EW-stellar parameter dependencies have been qualitatively proven in Chapter 17.5 of Hubeny & Mihalas (2014). Thus, to take into account such important dependencies in our codes, which can affect our derived abundances and thus our stellar parame-

ter derivation, we compute a Generalized Curve of Growth (GCOG) for each Fe I and Fe II line in our linelist. We define the GCOG for any given line i as:

$$\text{GCOG}_i: (T_{\text{eff}}, \log g, v_{\text{mic}}, \text{EW}) \mapsto A(\text{Fe})_i$$

A GCOG is thus a generalization of the well-known COG onto a higher dimensional mapping of $\text{EW} \mapsto A(\text{Fe})$. Alternatively, COG_i can be obtained by fixing T_{eff} , $\log g$ and v_{mic} for a given GCOG. GCOGs have been implemented in previous studies such as Osorio et al. (2015) and Boeche & Grebel (2016). We thus provide interpolated GCOGs which are stored as libraries in our code for every line in our linelist (see Section 2.1.4). The GCOGs are then utilized in the optimization module afterward to derive the Fe I and Fe II abundances.

2.3. Abundance Determination module

To derive the Fe I and Fe II abundances, we fit multivariate polynomials to the GCOG of each line, by deriving the relationship between the iron abundance of the line with T_{eff} , $\log g$, v_{mic} and EW, denoted as $A(\text{Fe}) = P(T_{\text{eff}}, \log g, v_{\text{mic}}, \text{EW})$. The detailed form of P

Table 1. Interpolation intervals chosen for different stellar types considered in LOTUS.

stellar parameter	types	intervals
T_{eff} (K)	K	[4000, 5200]
	G	[5200, 6000]
	F	[6000, 6850]
$\log g$	supergiant	[0.0, 0.5]
	giant	[0.5, 3.0]
	subgiant	[3.0, 4.0]
	dwarf	[4.0, 5.0]
[Fe/H]	very metal poor	[-3.5, -2.0]
	metal poor	[-2.0, -0.5]
	metal rich	[-0.5, 0.5]

can be written as:

$$\sum_{i_1+i_2+i_3+i_4 \leq n} a_{i_1 i_2 i_3 i_4} (T_{\text{eff}})^{i_1} (\log g)^{i_2} (v_{\text{mic}})^{i_3} (\text{EW})^{i_4} \quad (1)$$

where i_m ($m = 1, 2, 3, 4$) is the polynomial power of each of the 3 stellar parameters (T_{eff} , $\log g$ and v_{mic}) as well as EW. Possible values for i_m are positive integers, where the sum of all the powers should less than or equal to the power degree of the polynomial n . $a_{i_1 i_2 i_3 i_4}$ is the product of the polynomial coefficients of all the variables. The criteria for choosing n depends on the behavior of theoretical GCOG models within a range of stellar parameters and is described in more details in Section 2.3.1 below.

2.3.1. Selection of Interpolator

We choose the linelist utilized to derive stellar parameters to be dependent on the spectral type of the star, as some lines can be blended or strong in cool high metallicity stars, whereas these same lines could also be blend-free and weaker for hotter, metal-poor stars. Therefore, the multivariate polynomial functions defined in Section 2.3 used to derive the abundances determined from Fe I and Fe II lines depend on the choice of linelist for each spectral type. We

thus pay special attention to the choice of interpolator by identifying the best selection of linelist per spectral type (or stellar parameters). Therefore, instead of interpolating in the whole parameter space for all the lines, we pre-define that the GCOGs fit only the abundances determined from the lines we pre-selected and chose to use within tested intervals of stellar parameters, according to an initial guess of spectral types that the users can insert as an input in the code. Our choice of the intervals of different stellar parameters for each spectral types are listed in Table 1. For example, if an initial guess is chosen such that the target star is a metal-poor G giant, the multivariate polynomial will fit the abundance of each line versus other atmospheric parameters using the grid points falling into the range of T_{eff} from 5200 K to 6000 K, $\log g$ from 0.0 to 3.0 and [Fe/H] from -2.0 to -0.5.

In order to choose the best interpolator per spectral type (i.e., the optimal n) among several multivariate polynomials as defined in Equation 1, we use a Bayesian Information Criteria (BIC) to select the best polynomial function for each line based on the mean residual differences between the theoretical EWs at the nodes of our pre-computed NLTE grid (computed at a combination of T_{eff} , $\log g$, [Fe/H], and v_{mic}), to the EWs interpolated at these parameters. We assume that the optimal model is among the polynomials with degree=2,3,4,5. The BIC was calculated such as:

$$\text{BIC} = n \ln \left(\frac{\text{SSR}}{n} \right) + k \ln(n) \quad (2)$$

where SSR is the sum of the squared residuals between the theoretical EWs and the interpolated EWs from models at specific nodes of the grid, and n is sample size (here we choose $n = 4000$ nodes in each spectral type interval). k is a free parameter (including coefficients and slope intercept), which can be calculated as $k = C_{d+4}^d$, where d is the degree of the

polynomial, and 4 is chosen as the number of dependent variables for each interpolated EW (namely, T_{eff} , $\log g$, [Fe/H] and v_{mic}).

We thus chose the best interpolator for each spectral type interval as that with the lowest BIC value. In Fig. 3, we show the differences between the interpolated EW using the lowest BIC interpolator as compared to the (non-interpolated) EW directly from `MULTI2.3`, categorized as a function of stellar spectral types (x-axis) and metallicities (different panels). We observe that there exist no clear dependencies between differences and spectral types and metallicities. The average of differences is within 0.01 for all stellar spectral types and metallicities. We pre-define the default interpolated EW uncertainty (also a threshold for the lowest acceptable BIC) in `LOTUS` as $6 \text{ m}\AA$ for each line. However, we also design the code to allow users to input their acceptable uncertainty limits, in which case `LOTUS` will drop a given Fe I or Fe II from the linelist if the computed BIC is larger than this uncertainty, and will subsequently be excluded from the lines used to derive the stellar parameters in the optimization module.

2.3.2. EP Cut-off

The NLTE abundances derived from low excitation potential Fe I can yield larger abundances as compared with those derived from high-excitation Fe I and Fe II lines, especially using 1D atmospheric models (Amarsi et al. 2016). Such differences can reach up to 0.45 dex for some Fe I lines, and can affect our derived stellar parameters as documented in several studies including Bergemann et al. (2012); Lind et al. (2012) as well as others. We thus follow previous literature studies by introducing low-excitation potential cut-offs for Fe I lines with $\text{EP(Fe I)} < 2.7 \text{ eV}/2.5 \text{ eV}/2.0 \text{ eV}$ for stars with $[\text{Fe/H}] < -0.5$, depending on the number of Fe I and Fe II lines measured in the stars and the optimization convergence crite-

ria (see Section 2.4); We conduct no cut-offs for stars with $[\text{Fe/H}] > -0.5$.

2.4. Optimization Module

Once reliable linelist and interpolators per spectral types of input target stars have been chosen, as explained in Section 2.3 above, the derived iron abundances from Fe I and Fe II lines are fed into the optimization module with an initial guess of the general type of the target star. We note that users don't need to specify an initial guess of each stellar parameter, as it suffices to only chose an initial guess of the spectral type as an input to `LOTUS`, which is then assigned the corresponding interpolation parameters interval as indicated in Table 1.

2.4.1. Optimization Conditions

The general principle of optimization is to adjust stellar parameters iteratively to derive optimal combinations of stellar parameters that can satisfy the following three conditions: (i) excitation equilibrium, or minimizing the trend (i.e., slope) of the Fe I abundances as a function of excitation potential EP, (ii) ensuring ionization equilibrium or minimizing the differences between the abundances derived from the Fe I and Fe II lines, and (iii) minimizing the trend (i.e., slope) between the abundances derived from the Fe I lines versus the reduced equivalent widths, $\text{REW} = \log(\text{EW}/\lambda)$.

Therefore, we derive T_{eff} by ensuring excitation equilibrium, $\log g$ by ensuring ionization equilibrium, and v_{mic} by minimizing the trend between Fe I abundances versus line strength (REW). [Fe/H] was then determined by averaging the abundances derived from the Fe I and Fe II abundances.

2.4.2. Targeted Optimized Object Function

In order to find the best combination of stellar parameters that satisfy the optimization conditions defined in Section 2.4.1 within our parameter grid, we first combine these conditions into

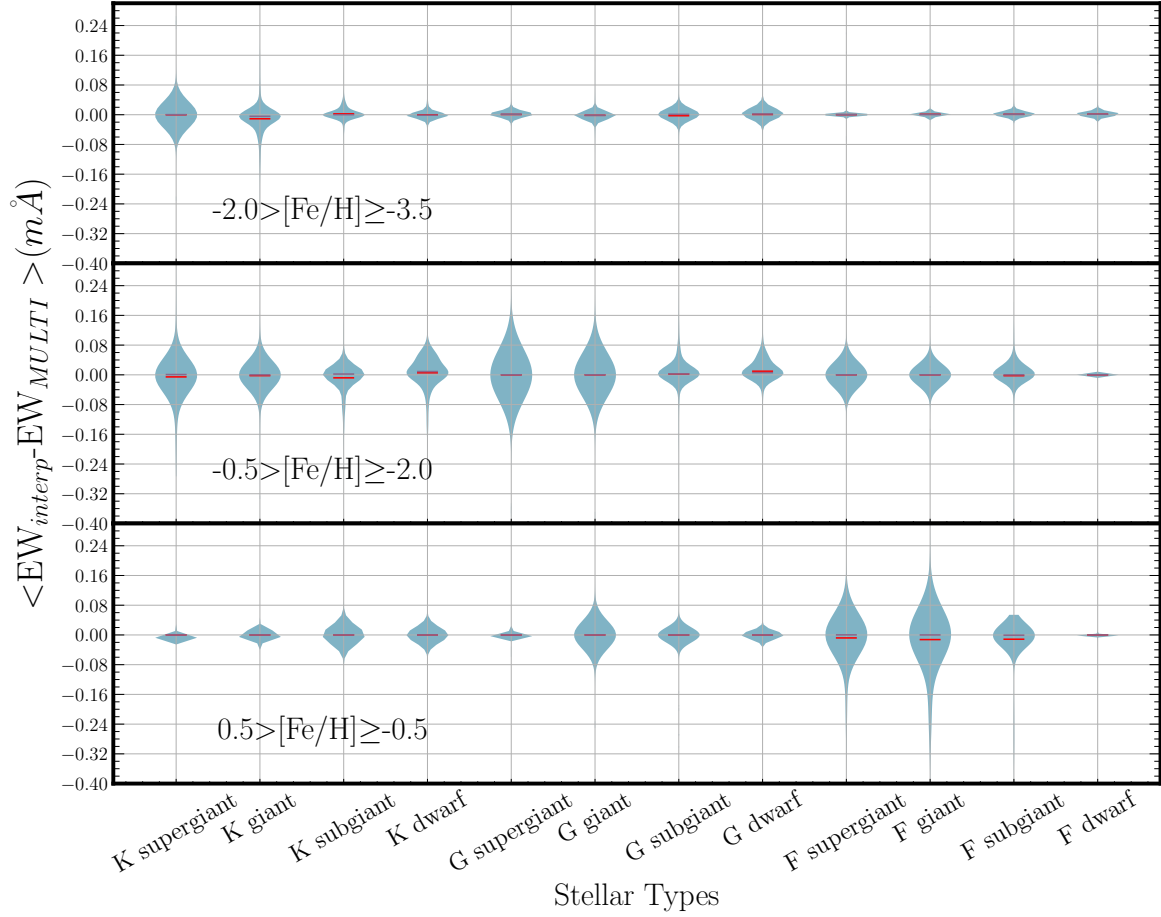


Figure 3. Differences (in mÅ) between the interpolated EWs (using interpolators chosen at the lowest BIC values) and the EWs from NLTE theoretical calculations computed directly using `MULTI2.3`. Each violin plot shows the distribution of the means of such differences for a random 4000 nodes within the spectral type interval of the pre-computed EW library. Red lines are marked as the means of the distributions while purple lines are for the medians. The differences are shown for different metallicity ranges as indicated in each panel.

an object function \mathcal{F} , such as:

$$\mathcal{F} = \left(\frac{s_{\chi,1}}{\sigma_{\chi,1}} \right)^2 + \left(\frac{s_{REW,1}}{\sigma_{REW,1}} \right)^2 + \left(\frac{\bar{A}_1 - \bar{A}_2}{\sigma_{1-2}} \right)^2 \quad (3)$$

where the subscripts "1" and "2" correspond to Fe I and Fe II, respectively. $s_{\chi,1}$ is the slope between Fe I abundances and EP, and $\sigma_{\chi,1}$ is its uncertainty, $s_{REW,1}$ is the slope between the Fe I abundances and REW, and $\sigma_{REW,1}$ is its uncertainty. \bar{A}_1 and \bar{A}_2 are the mean abundances for Fe I and Fe II, respectively, while σ_{1-2} is the standard deviation of the differences between \bar{A}_1 and \bar{A}_2 . A converged solution is obtained at

the combination of T_{eff} , $\log g$, $[\text{Fe}/\text{H}]$ and v_{mic} , which minimizes \mathcal{F} globally.

2.4.3. Global minimization

To find the global minimization fit parameters within our grid, we adopt a differential evolution algorithm implementing a global minimization search. The goal is to minimize \mathcal{F} by starting with an initial population of candidate solutions, which are iteratively improved by retaining the fittest solutions that yield a lower \mathcal{F} values, until convergence for the best-fit parameters is met (Storn & Price 1996). The advantage of a differential evolution algorithm is that

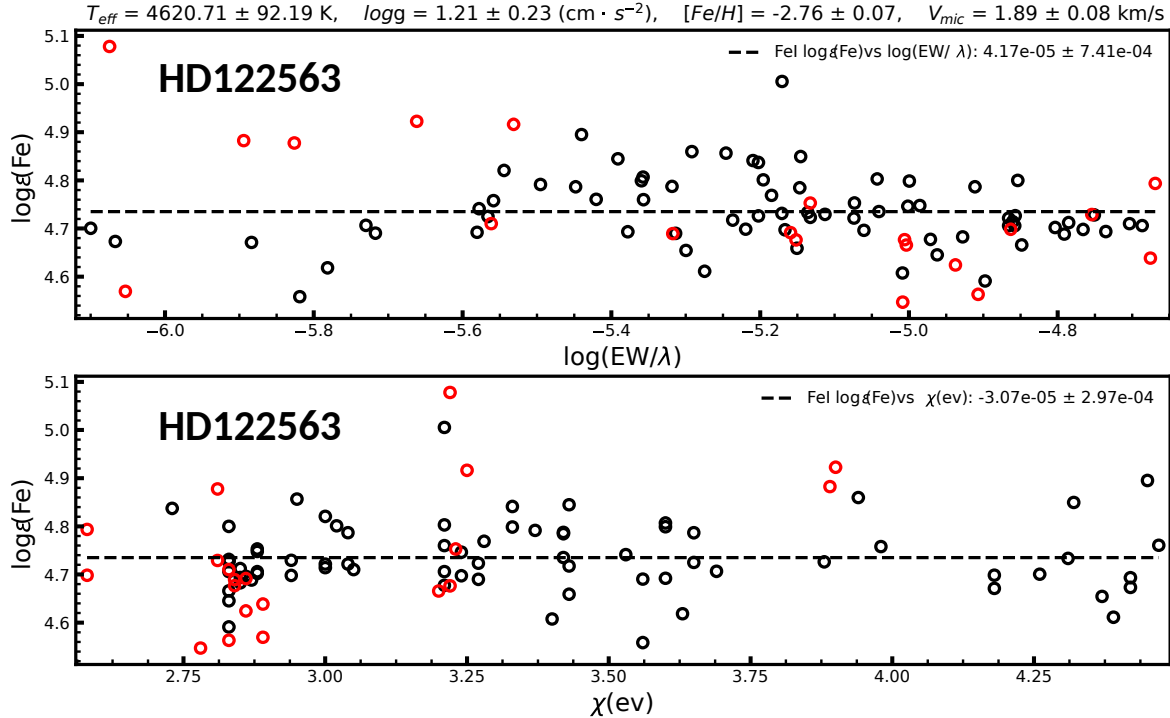


Figure 4. Iron abundances determined from Fe I (black circles) and Fe II (red circles) line versus reduced equivalent widths (upper panel) and excitation potential energies χ (lower panel) for selected lines in the metal-poor benchmark star HD122563. The parameters indicated on the top are the optimal values derived using the global minimization (differential evolution) algorithm in LOTUS. Dotted lines are the best linear fits to the Fe I lines in each panel. The labels at the upper left corner of each panel are the slopes of the fits and their corresponding standard deviations.

it has the benefit of handling nonlinear and non-differentiable multi-dimensional objective functions while requiring few control parameters to steer the minimization. For our code, we select 100 initial populations (sets of solutions) with a combined rate of 0.3, which is a crossover probability that depends on how fast the algorithm moves to the next generation of populations. We try different weights between 0.8 and 1.2, to maintain a proper searching radius, at the same time making sure it does not slow down the convergence speed. We adopt $\mathcal{F} \sim 10^{-5}$ as the absolute tolerance for each iteration. After each iteration, we perform a 3σ -clipping on the abundances determined from the Fe I and Fe II lines to remove outliers. We adopt 3 iterations of outlier removing in total as a default, however, this number can be defined by the users depending on the quality of their EW measure-

ments. An example of HD122563 with derived abundances of Fe I and Fe II versus REW and EP at optimal atmospheric parameters is shown in Figure 4.

2.5. Uncertainty Estimation Module

Since \mathcal{F} is a function of the stellar parameters, it can be described as $\mathcal{F}(\theta) = \mathcal{F}(T_{\text{eff}}, \log g, v_{\text{mic}})$. We can keep track of how \mathcal{F} changes along the perturbations around the optimal solution $\theta^* = (T_{\text{eff}}^*, \log g^*, v_{\text{mic}}^*)$. T_{eff}^* , $\log g^*$ and v_{mic}^* are the parameters at the optimal solution. Indeed, \mathcal{F} resembles a likelihood function, which can be used to estimate the uncertainties on each of our derived stellar parameters from the Hessian Matrix such as:

$$SE(\theta^*) = \text{diag}(\sqrt{\mathcal{H}^{-1}(\theta^*)}) \quad (4)$$

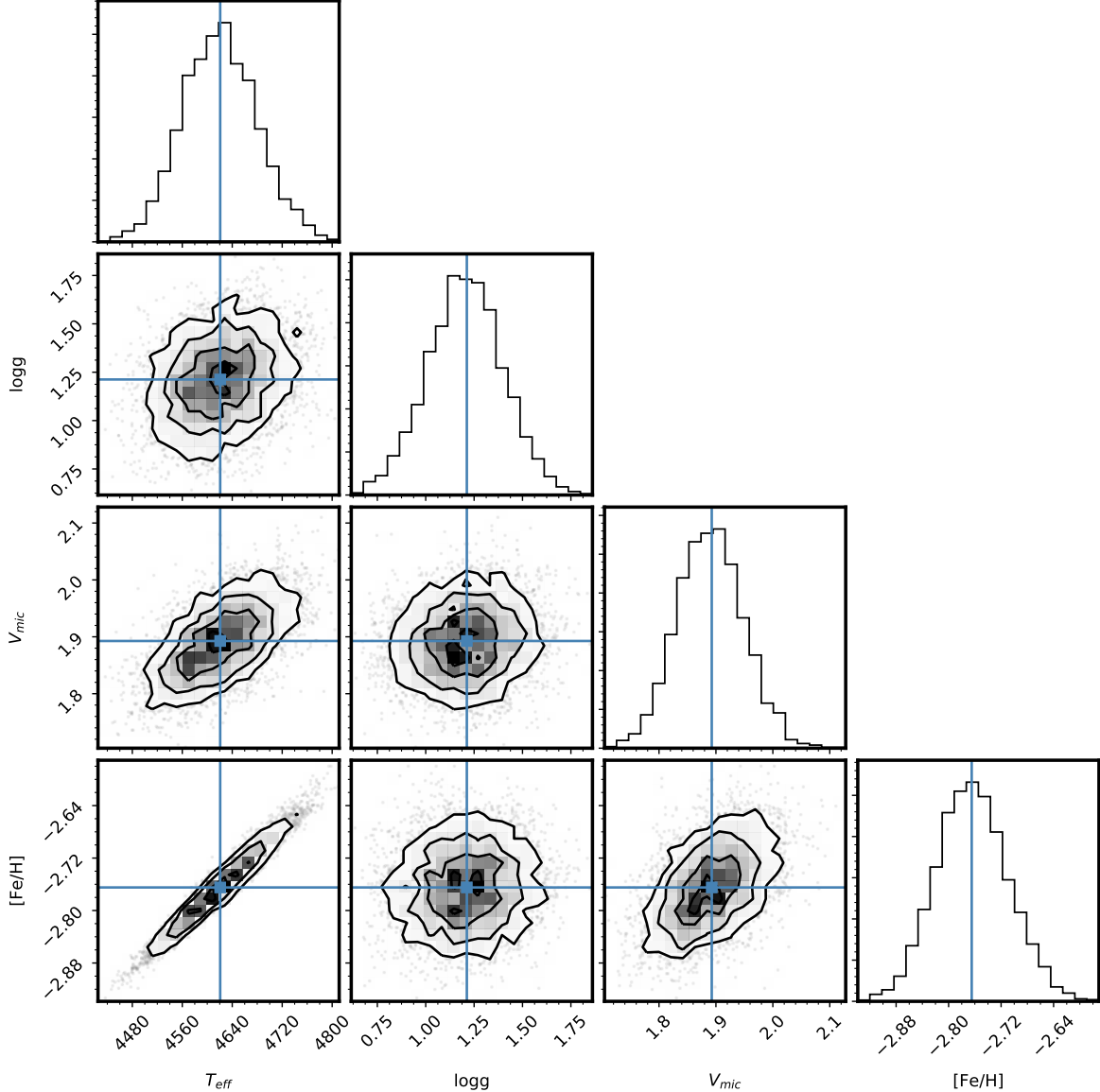


Figure 5. Marginalized posterior distributions of the stellar parameters of HD122563 based on the log-likelihood function in Equation 6. 1σ , 2σ and 3σ uncertainty region are denoted as solid contours in the two dimensional plot. The histograms show the marginalized posterior distributions for each parameter, respectively. Blue intersecting lines show the values obtained from our global optimization module.

where the Hessian Matrix for our objective function can be written as:

$$\mathcal{H}(\theta) = \frac{\partial}{\partial \theta_i \partial \theta_j} \mathcal{F}(\theta), 1 \leq i, j \leq 3 \quad (5)$$

For $[\text{Fe}/\text{H}]$, we adopt the standard deviation of the Fe I lines as the uncertainty.

However, in the above uncertainty framework, one strong assumption is that the standard errors obtained are symmetric around the mean

values. This is only true if the probability distribution function of the derived parameters is a normal distribution. Normally, this is not the case. We, therefore, use a Bayesian framework to robustly determine the uncertainties on our derived stellar parameters. First, we construct a log-likelihood function using the same terms as in Equation 3 such as:

$$\log(\mathcal{L}) = -\frac{1}{2} \sum_{i \leq 3} \left[\left(\frac{s_i}{n_i} \right)^2 + \log(2\pi n_i) \right] \quad (6)$$

where n_i can be written as:

$$n_i = \sigma_i^2 + f^2 s_i^2 \quad (7)$$

where s_i represent the slopes $s_{\chi,1}$, $s_{REW,1}$ and $\bar{A}_1 - \bar{A}_2$ individually, while σ_i are their corresponding standard deviations. Introducing f will compensate the underestimation of the variance of each parameter assuming such an additional term is proportional to the model itself.

We then perform the Slice Sampling algorithm (Neal 2003), which is a type of Markov Chain Monte Carlo (MCMC) implemented in PyMC3, to complete the estimation of the posterior probability of each parameter. This method adjusts the step size automatically on every proposed candidate to match the profile of the posterior distribution without the need to choose a transition function. Such a framework ensures higher efficiency as compared to classical MCMC algorithms, such as Metropolis and Gibbs (Metropolis & Ulam 1949; Geman & Geman 1984). For all stellar parameters, we derive a normal distribution around the mean optimized value obtained from the global minimization module described in Section 2.4.3, and a standard deviation determined from the standard errors of the Hessian Matrix.

We use the logarithmic of f as an input variable to the MCMC sampler with a uniform distribution ranging from -10 to 1 . In the sampling process, we consider 4 running chains with each containing 1000 draw steps and 200 tunes steps. Figure 5 shows the output from our posterior distribution of the stellar parameters and their uncertainty regions for a benchmark metal-poor star, HD122563. On the same plot, we also show the optimized parameters derived using our global optimization module (blue lines intersection), which agree very well.

3. TESTING LOTUS

We test LOTUS by deriving the atmospheric stellar parameters of benchmark stars with well

constrained non-spectroscopic and fundamental stellar parameters, to quantify the precision of our derived parameters and their uncertainties. Below we present the results of these tests. We list the derived stellar parameters (T_{eff} , $\log g$, [Fe/H] and v_{mic}) using LOTUS in LTE and NLTE of all the stars considered from Section 3.1 to 3.4 below, the sources of the EW, the number of Fe I and Fe II lines, and the excitation potential cut-offs for each star in Table 3.

3.1. HD122563, HD140283, and Arcturus

The two metal-poor standard stars HD122563, HD140283 and the benchmark giant Arcturus have been widely analyzed independently in the literature. Their stellar parameters have therefore been derived spectroscopically (using 1D, 3D, LTE and NLTE assumptions, or a combination of each), as well as using non-spectroscopic methods and fundamental equations (e.g., using photometric calibrations, asteroseismology, or interferometric angular diameters). All three stars are dubbed benchmark stars which have been selected as comparison standards for the largest stellar surveys, especially in the *Gaia*-ESO spectroscopic survey (Jofré et al. 2014; Heiter et al. 2015). We adopt EW measurements of each benchmark star from literature publications as follows: HD122563 (Frebel et al. 2013), HD140283 (Frebel et al. 2013), Arcturus (Jofré et al. 2014). Frebel et al. (2013) measured their EW from high-resolution spectroscopic observations ($R \sim 35,000$ in the blue and $\sim 28,000$ in the red) of HD122563 and HD140283, obtained with the MIKE spectrograph (Bernstein et al. 2003) on the Magellan-Clay telescope at Las Campanas. A $R \geq 70,000$ spectrum was used to derive EW for Arcturus from the VLT spectrum (Jofré et al. 2014). We derive the stellar parameters of each star and their uncertainties using LOTUS. We then compare our NLTE and LTE parameters with several independent de-

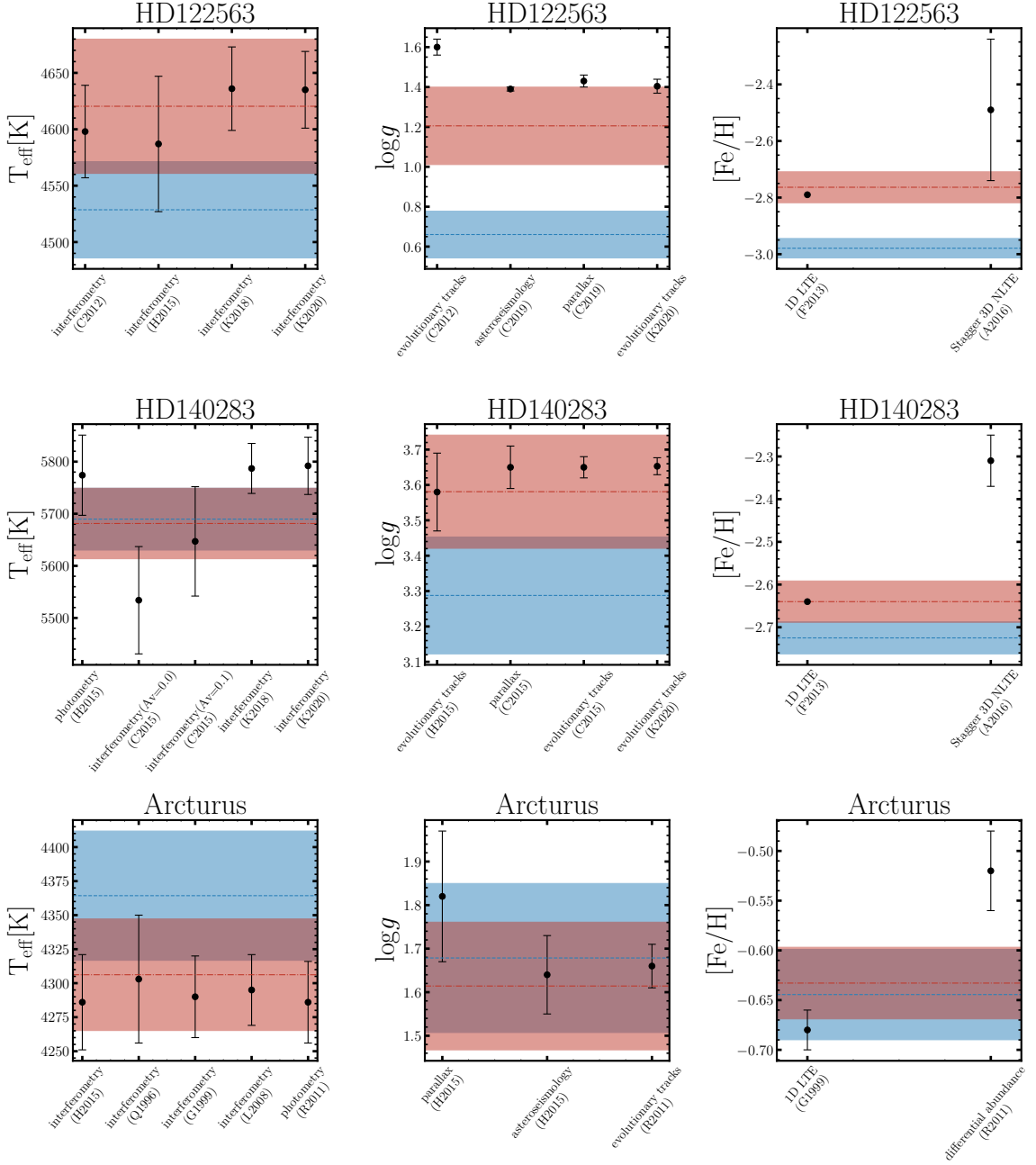


Figure 6. Comparison of our derived stellar parameters, T_{eff} , $\log g$ and $[\text{Fe}/\text{H}]$ using **LOTUS** to reference literature values derived non-spectroscopically (for T_{eff} and $\log g$) for HD122564, HD140283 and Arcturus. The mean NLTE values (red dashed lines) with their 1σ confidence intervals (red shadow areas) and our mean LTE values (blue dashed lines) with their 1σ confidence intervals (blue shadow areas), compared to to reference stellar parameters (black dots with error bars) for references on the x-axis. References are as follows: Q1996...Quirrenbach et al. (1996); G1999...Griffin & Lynas-Gray (1999); L2008...Lacour et al. (2008); R2011...Ramírez & Allende Prieto (2011); C2012...Creevey et al. (2012); F2013...Frebel et al. (2013); H2015...Heiter et al. (2015); C2015...Creevey et al. (2015); A2016...Amarsi et al. (2016); K2018...Karovicova et al. (2018); C2019...Creevey et al. (2019); K2020...Karovicova et al. (2020).

terminations from the literature, as shown in Figure 6.

HD122563—We derive $T_{\text{eff}} = 4620 \pm 59$ K, $\log g = 1.21 \pm 0.19$, $v_{\text{mic}} = 1.89 \pm 0.06$ km s⁻¹

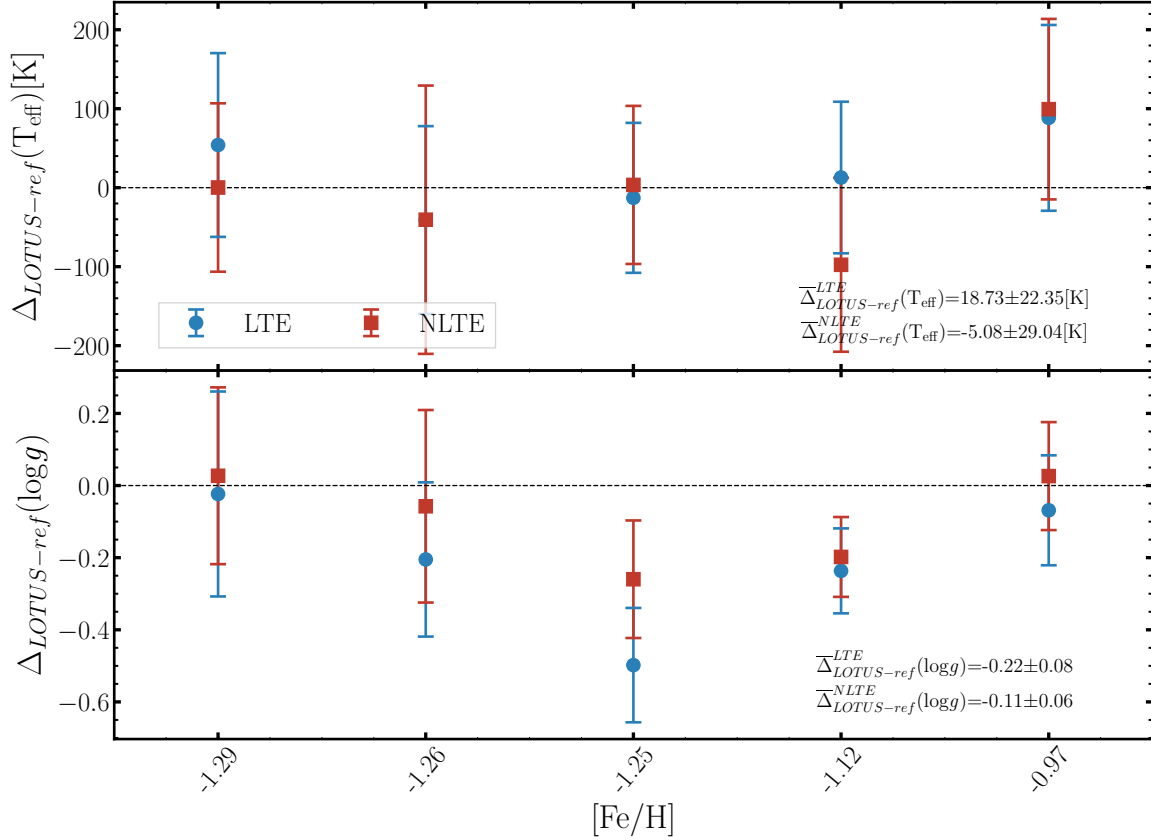


Figure 7. Differences in $\log g$ and T_{eff} between values derived using LOTUS versus reference values from Hawkins et al. (2016) for five GES metal-poor stars in their sample. Blue circles are LTE differences, while red squares are NLTE. Dashed lines in both panels are the zero baselines. Average systematic offsets are included in the text of each panel.

and $[\text{Fe}/\text{H}] = -2.76 \pm 0.05$ in NLTE, and $T_{\text{eff}} = 4528 \pm 42$ K, $\log g = 0.66 \pm 0.12$, $v_{\text{mic}} = 1.84 \pm 0.03$ km s $^{-1}$ and $[\text{Fe}/\text{H}] = -2.98 \pm 0.03$. Creevey et al. (2012) derived $T_{\text{eff}} = 4598 \pm 41$ K using an angular diameter observed with CHARA interferometry and Palomar interferometric observations. Heiter et al. (2015) derived $T_{\text{eff}} = 4587 \pm 60$ K based on the angular diameters and bolometric flux calibrations, and $\log g = 1.44 \pm 0.24$ from fitting evolutionary tracks. Karovicova et al. (2018) updated CHARA interferometry with more data and derived an effective temperature of $T_{\text{eff}} = 4636 \pm 37$ K. Later in Karovicova et al. (2020), they updated their data reduction pipeline and derived a new $T_{\text{eff}} = 4635 \pm 34$ K. Our NLTE T_{eff} derived for HD122563 agrees

very well with T_{eff} determined in these studies using interferometric angular diameters, within ~ 30 K, while the LTE T_{eff} deviated by ~ 100 K from the reference values.

And for $\log g$ results from the recent updated asteroseismic analysis are in agreement with the NLTE values in our work, which is close to the upper limit of 1σ confidence interval.

For $\log g$, Creevey et al. (2012) used evolutionary track models to derive $\log g = 1.60 \pm 0.04$ for HD122563, while Creevey et al. (2019) utilized the Hertzsprung telescope (SONG network node) to accurately measure the surface gravity of HD122563 using asteroseismology for the first time, and derived $\log g = 1.39 \pm 0.01$. In their paper they also compare to *Gaia* DR2 parallax-based $\log g = 1.43 \pm 0.03$, which shows high con-

sistency between these methods. Karovicova et al. (2020) also used evolutionary track models to derive $\log g = 1.404 \pm 0.03$ for the same star. Our LOTUS $\log g = 1.22$ in NLTE matches within ~ 0.1 dex the asteroseismic and parallax $\log g$ in Creevey et al. (2019), whereas the LTE value is 0.6 dex lower. This gives us strong confidence in LOTUS' ability to derive NLTE surface gravities from spectroscopic observations.

We then compare our NLTE and LTE [Fe/H] with those derived by Frebel et al. (2013) in 1D, LTE and Amarsi et al. (2016) in 3D,NLTE. Our NLTE [Fe/H] agrees with that determined in both studies within error bars, although Amarsi et al. (2016) derived a higher [Fe/H] = -2.5 , which is likely due to considering 3D effects in their study.

HD140283—We derive $T_{\text{eff}} = 5681 \pm 67$ K, $\log g = 3.58 \pm 0.16$, $v_{\text{mic}} = 2.17 \pm 0.16$ km s $^{-1}$ and [Fe/H] = -2.64 ± 0.05 in NLTE, and $T_{\text{eff}} = 5689 \pm 59$ K, $\log g = 3.29 \pm 0.17$, $v_{\text{mic}} = 2.09 \pm 0.14$ km s $^{-1}$ and [Fe/H] = -2.72 ± 0.04 in LTE. Heiter et al. (2015) derived a mean $T_{\text{eff}} = 5774 \pm 77$ K for the sub-giant in their *Gaia*-ESO benchmark sample from photometric calibrations. Additionally, Creevey et al. (2015) used the VEGA interferometer on CHARA to determine $T_{\text{eff}} = 5534 \pm 103$ K (using $A_V = 0.0$ mag) and $T_{\text{eff}} = 5647 \pm 105$ K (using $A_V = 0.1$ mag). Karovicova et al. (2018) similarly derived an updated $T_{\text{eff}} = 5787 \pm 48$ K from additional interferometric data points, and afterwards updating their values to 5792 ± 55 K in Karovicova et al. (2020). Our LTE and NLTE T_{eff} for HD140283 agree with the interferometric values derived in Creevey et al. (2015) within 120 K and Karovicova et al. (2018, 2020) within 80 K.

Heiter et al. (2015) derived $\log g = 3.58 \pm 0.11$ using fundamental relations and adopting independently derived parallax for the star. Creevey et al. (2015) also derived a mean $\log g = 3.69 \pm 0.03$, similarly from a combination of parallax and evolutionary track mod-

els. Both $\log g$ determined by parallax methods in Heiter et al. (2015) and Creevey et al. (2015) agree well with our NLTE value to within 0.05 dex. Karovicova et al. (2020) derived $\log g = 3.65 \pm 0.0$ from evolutionary models. Our LTE values is, unexpectedly, 0.3 dex lower.

Similar to HD122563, we compare our [Fe/H] with 1D,LTE and 3D,NLTE abundances in Frebel et al. (2013) and Amarsi et al. (2016), respectively. Given that both studies derived their abundances by fixing T_{eff} and $\log g$, while ours were derived simultaneously using the global optimization method adopted in LOTUS, we warrant serious direct comparison with their values. Nevertheless, our NLTE values agree very well with that derived in Frebel et al. (2013) within 1σ , whereas is 0.3 dex lower as compared to Amarsi et al. (2016).

Arcturus—We derive $T_{\text{eff}} = 4306 \pm 41$ K, $\log g = 1.61 \pm 0.15$, $v_{\text{mic}} = 1.79 \pm 0.02$ km s $^{-1}$ and [Fe/H] = -0.63 ± 0.04 in NLTE, and $T_{\text{eff}} = 4364 \pm 47$ K, $\log g = 1.68 \pm 0.17$, $v_{\text{mic}} = 1.76 \pm 0.02$ km s $^{-1}$ and [Fe/H] = -0.64 ± 0.05 in LTE. For T_{eff} Quirrenbach et al. (1996) used the MkIII Optical Interferometer on Mt. Wilson to determine Arcturus' angular diameter and derived $T_{\text{eff}} = 4303 \pm 47$ K. Griffin & Lynas-Gray (1999) collected all literature results of interferometry observation up to their study and derived $T_{\text{eff}} = 4290 \pm 30$ K. Lacour et al. (2008) used the IOTA 3 telescope interferometer in the H band to derive $T_{\text{eff}} = 4295 \pm 26$ K. Additionally, Ramírez & Allende Prieto (2011) fit theoretical spectral energy distributions (SED) from visible blue bands to mid-infrared to derive $T_{\text{eff}} = 4286 \pm 30$ K. Finally, Heiter et al. (2015) derived a mean of 4274 ± 83 K from different interferometric measurements, even though they warranted against using Arcturus as a benchmark given the large dispersion they obtained. All interferometric T_{eff} agree very well with our

NLTE T_{eff} to within ~ 20 K. Our LTE value is, however, ~ 80 K higher.

Ramírez & Allende Prieto (2011) derived $\log g = 1.66 \pm 0.05$ from HIPPARCOS parallax and isochrone fitting, while Heiter et al. (2015) derived a fundamental $\log g = 1.64 \pm 0.09$ based on seismic mass and $\log g = 1.82 \pm 0.15$ from a compilation of parallax-based measurements. Our NLTE $\log g$ agrees very well with both results, whereas our LTE values is 0.1 dex higher.

Griffin & Lynas-Gray (1999) derived $[\text{Fe}/\text{H}] = -0.68 \pm 0.02$ by comparing theoretical 1D, LTE SEDs with observed flux. Ramírez & Allende Prieto (2011) used a differential abundance analysis relative to the solar spectrum to derive $[\text{Fe}/\text{H}] = -0.52 \pm 0.04$. Our NLTE and LTE $[\text{Fe}/\text{H}]$ are within 0.05 dex from each other, and agree well with the values derived in Griffin & Lynas-Gray (1999) while being ~ 0.1 dex as compared to differential abundance analysis in Ramírez & Allende Prieto (2011).

3.2. GES Metal-Poor Stars

We also test LOTUS on five metal-poor benchmark stars proposed by Hawkins et al. (2016) from the *Gaia*-ESO survey (GES). They determined T_{eff} via the Infrared Flux Method (IRFM) (Casagrande et al. 2011) using multi-band photometry and $\log g$ by fitting to evolutionary stellar models. The Fe I and Fe II EWs for the sample stars were adopted from Hawkins et al. (2016), who used different EW measurements from different pipelines from the GES survey to derive their parameters. We use their EPINARBO (EPI) EWs derived with the FAMA pipeline following Magrini et al. (2013), as those were derived consistently. We compare our derived T_{eff} and $\log g$ using LOTUS to those in Hawkins et al. (2016) using the same Fe I and Fe II lines. We find that our NLTE parameters are on average within 5 ± 29 K from their T_{eff} and 0.11 ± 0.06 for $\log g$ on average, whereas our LTE parameters are within 18 ± 22 K and 0.22 ± 0.08 dex for T_{eff} and $\log g$ respectively.

Star by star comparisons are shown in Figure 7. Our NLTE parameters agree better with the non-spectroscopic parameters from Hawkins et al. (2016), as compared to LTE.

A larger $\log g$ dispersion is obtained for HD106038 though with $[\text{Fe}/\text{H}] = -1.25$ of -0.25 and -0.45 , for both our NLTE and LTE results, respectively. With a 3D, Non-LTE analysis, and *Gaia* EDR3 parallax, Giribaldi et al. (2021) derived $\log g = 4.29 \pm 0.04$, which is in excellent with our NLTE $\log g = 4.29 \pm 0.08$. Additionally, only 35 Fe I lines used by Hawkins et al. (2016) were used to derive the stellar parameters in LOTUS which decreases the accuracy of optimal values (see Section 5 for more details).

3.3. GES-K2 Stars

We also test LOTUS by deriving atmospheric stellar parameters of a sample of Kepler-2 (K2) star sample, which was also observed using a high-resolution UVES spectrograph on the VLT as part of the GES survey. Worley et al. (2020) combined the high-resolution spectroscopic observations from UVES, photometry, and precise asteroseismic data from K2 to derive self-consistent stellar parameters for these stars, which represent a good non-spectroscopic sample to compare our stellar parameters derived with LOTUS to.

We adopt the EW measurements from Worley et al. (2020) derived from high-resolution UVES spectroscopic observations. We chose a total of 52 stars from their sample. The majority of the stars in the sample are metal-rich with $[\text{Fe}/\text{H}] > -0.5$. Only six stars have $[\text{Fe}/\text{H}] < -0.5$. Worley et al. (2020) used the IRFM to determine photometrically calibrated T_{eff} for all their stars following Casagrande et al. (2010, 2011).

The average uncertainties reported in Worley et al. (2020) for T_{eff} and $\log g$ of the GES-K2 stars are ± 65 K and ± 0.02 , respectively. We note that these values are close to our parameter grid resolution. We derive the stellar pa-

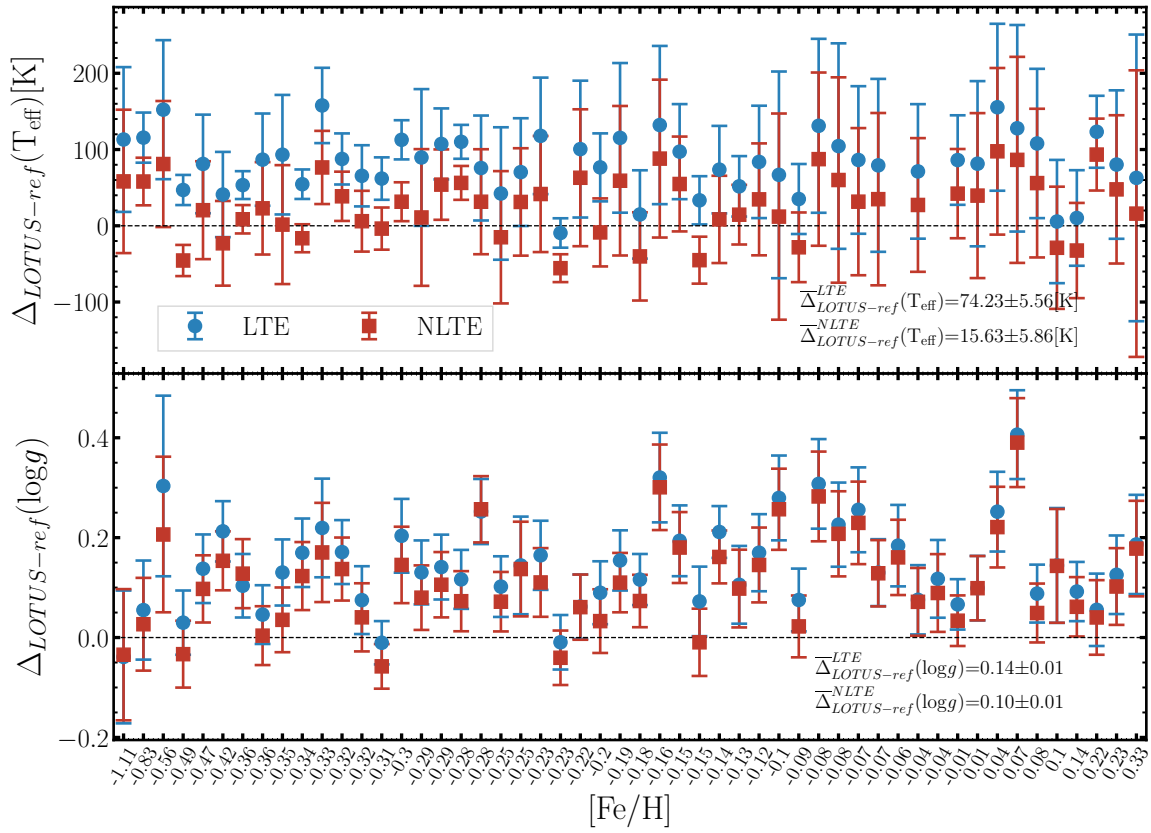


Figure 8. Same as in Figure 7 for the GES-K2 sample stars from Worley et al. (2020).

rameters for the 52 GES-K2 stars using LOTUS. Our results for $\log g$ and T_{eff} as compared to Worley et al. (2020) are shown in Figure 8 as a function of $[\text{Fe}/\text{H}]$. We find that the average differences between the LOTUS parameters are $\bar{\Delta}T_{\text{eff}} = 74 \pm 6$ K and $\bar{\Delta}\log g = 0.14 \pm 0.01$ in LTE, and $\bar{\Delta}T_{\text{eff}} = 16 \pm 6$ K, $\bar{\Delta}\log g = 0.10 \pm 0.01$ in NLTE. Both LTE and NLTE parameters agree well with the photometric and asteroseismic parameters from Worley et al. (2020) within their error bars, however our NLTE parameter derivations agree better for both T_{eff} and, particularly for $\log g$.

3.4. CHARA Interferometry Stars

Finally, we apply and test LOTUS on a sample of stars with effective temperatures derived homogeneously from interferometric angular diameters observed by CHARA from Karovicova et al. (2020, 2021a,b). Karovicova et al. (2020) presented a study of interferometric ob-

servations of ten late-type metal-poor dwarfs and giants, whereas Karovicova et al. (2021a,b) showed a similar analysis for several metal-rich stars. For three of their stars (namely, HD122563, HD140283, and HD175305), we have already presented their analysis in Section 3.1 and 3.2. We, therefore, do not include the analysis of these stars again in this section. EW measurements of the total 12 stars were adopted from different literature sources including Takeda et al. (2005); Morel et al. (2014); Heiter et al. (2015); Takeda & Tajitsu (2015); Liu et al. (2020). The average uncertainties of the interferometric T_{eff} estimated by Karovicova et al. (2020, 2021a,b) are within 1%. The authors derived their $\log g$ values by fitting Dartmouth isochrones (Dotter et al. 2008) to their interferometric T_{eff} . They thus derive median uncertainties for $\log g$ of 0.09 for their metal-

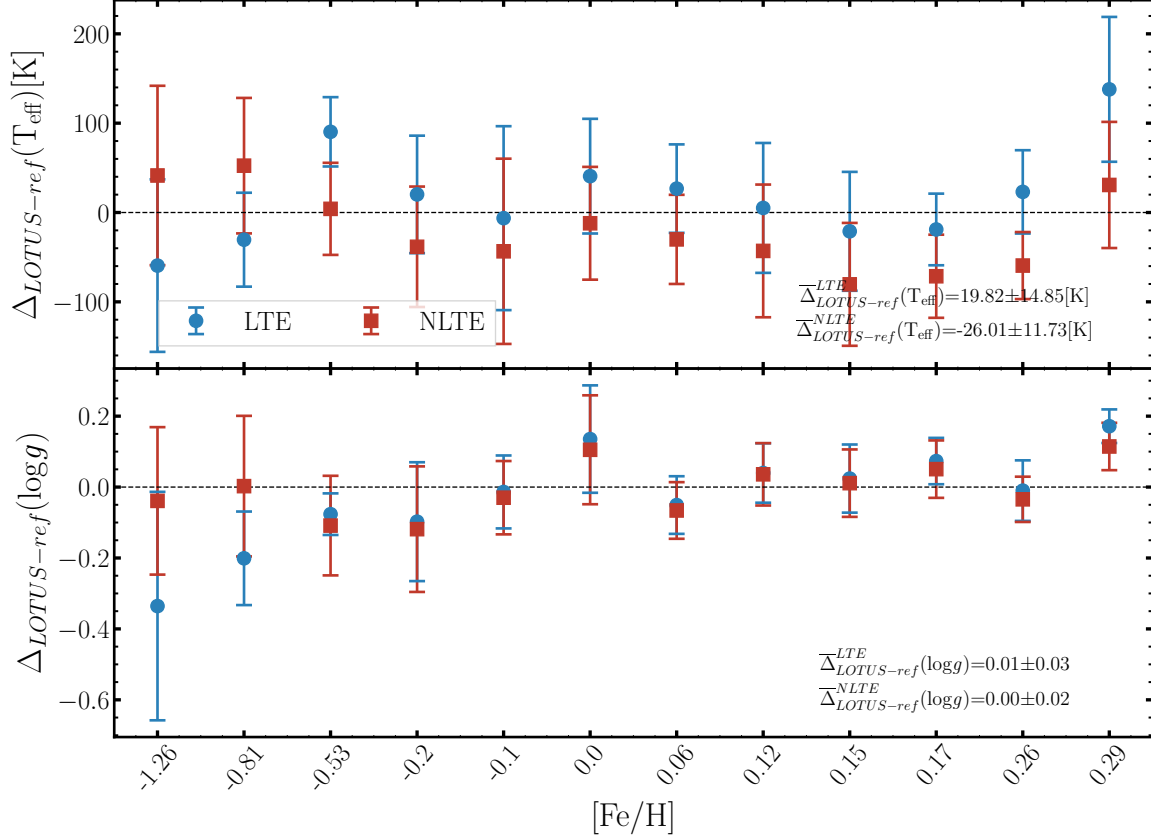


Figure 9. Same as in Figure 7 for the CHARA sample stars from Karovicova et al. (2020, 2021a,b).

poor star sample, 0.05 for their dwarf sample, and 0.07 for the giants/subgiants sample.

We find that on average the differences in T_{eff} and $\log g$ between the reference values (Karovicova et al. 2020, 2021a,b) and those derived with LOTUS are within 26 K and 0.01 in NLTE, respectively. The NLTE parameters derived for all the stars agree within 1σ as compared to the reference values, except for the $\log g$ value of HD121370 with $[\text{Fe}/\text{H}] = 0.29$, which deviated by 0.12 for LTE and 0.18 for NLTE. Heiter et al. (2015), however, reported a seismic $\log g$ for this star of 3.83 ± 0.02 dex, which agrees very with our NLTE result of 3.91 ± 0.06 within 1σ .

4. NLTE CORRECTIONS

The stars presented in Section 3 for testing LOTUS on benchmark stars with T_{eff} and $\log g$ derived using non-spectroscopic methods cover a limited range of metallicities (mostly with $[\text{Fe}/\text{H}] > -1.0$), as well as mainly dwarfs and

sub-giant stars. However, NLTE stellar parameter “corrections” (also known as NLTE effects, defined as $\Delta_{\text{NLTE}} = \text{parameter}(\text{NLTE}) - \text{parameter}(\text{LTE})$) have been shown in the literature to be more significant and important for evolved (giants and supergiant) metal-poor stars Lind et al. (2012); Ezzeddine et al. (2017). Thus, to be able to test our derived NLTE “corrections” on a larger, more metal-poor sample of giant stars, we derive LTE and NLTE stellar parameters for the *R*-process Alliance giant metal-poor star sample from Hansen et al. (2018), who derived the stellar parameters of 107 metal-poor stars ($[\text{Fe}/\text{H}] < -1.0$) selected based on their *r*-process enhancement from several surveys. The EW measurements for Fe I and Fe II lines were adopted from Hansen et al. (2018), measured from their du Pont spectroscopic observations. We thus add the RPA sample stars to our test sample stars presented in Section 3, resulting in

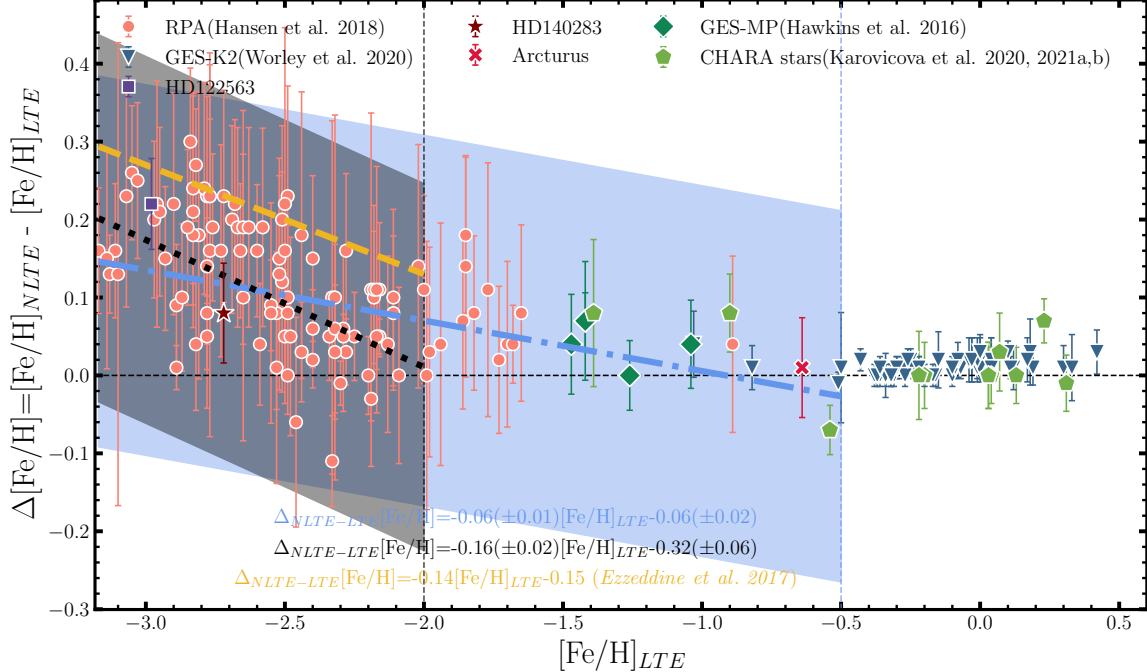


Figure 10. NLTE corrections $\Delta[\text{Fe}/\text{H}]$ versus $[\text{Fe}/\text{H}]_{\text{LTE}}$ determined for this work’s star sample using LOTUS. Different markers indicate stars from different studies as indicated. The Yellow dashed line is a linear fit from Ezzeddine et al. (2017) for stars with $[\text{Fe}/\text{H}] < -4.0$. The Blue dot-dash line is our fit to the stars for $[\text{Fe}/\text{H}] < -0.5$, and the black dotted line is our fit to the stars with $[\text{Fe}/\text{H}] < -2.0$.

a significant sample covering a wide representative range of stellar parameters from $T_{\text{eff}}=4000$ to 6500 K, $\log g=0.0$ to 4.5, and $[\text{Fe}/\text{H}]=-3.0$ to -0.5 . The derived stellar parameters for the RPA stars, in LTE and NLTE, are also listed in Table 3.

We derive the NLTE corrections for $[\text{Fe}/\text{H}]$ (denoted as $\Delta[\text{Fe}/\text{H}]$) for the full sample of stars. We plot the results as a function of $[\text{Fe}/\text{H}]_{\text{LTE}}$ in Figure 10. As expected, $\Delta[\text{Fe}/\text{H}]$ increases toward lower metallicities. Such effects have been shown in multiple previous studies as well (for e.g., Mashonkina et al. 2011; Lind et al. 2012; Bergemann et al. 2012; Amarsi et al. 2016; Ezzeddine et al. 2017). Ezzeddine et al. (2017) derived a linear relation between the NLTE correction for $[\text{Fe}/\text{H}]$, $\Delta[\text{Fe}/\text{H}]$, and $[\text{Fe}/\text{H}]_{\text{(LTE)}}$ from 20 ultra metal-poor stars with $[\text{Fe}/\text{H}] < -4.0$, such as:

$$\Delta[\text{Fe}/\text{H}] = -0.14[\text{Fe}/\text{H}]_{\text{LTE}} - 0.15 \quad (8)$$

They found that their relationship can also be extended for metal-poor benchmark stars at $-4.0 < [\text{Fe}/\text{H}] < -2.0$. It is therefore useful to re-derive this equation using our full stellar sample analyzed uniformly using LOTUS, for comparison. Following Ezzeddine et al. (2017), we re-derive the relation between $\Delta[\text{Fe}/\text{H}]$ and $[\text{Fe}/\text{H}]_{\text{(LTE)}}$ using our sample of stars. We re-derive the relation by (i) choosing only the stars with $[\text{Fe}/\text{H}]_{\text{(LTE)}} < -0.5$, and (ii) using the stars with $[\text{Fe}/\text{H}]_{\text{(LTE)}} < -2.0$. We thus derive $\Delta[\text{Fe}/\text{H}] =$

$$\begin{cases} -0.06(\pm 0.01)[\text{Fe}/\text{H}]_{\text{LTE}} - 0.06(\pm 0.02), \\ \text{for } [\text{Fe}/\text{H}]_{\text{LTE}} < -0.5 \\ -0.16(\pm 0.02)[\text{Fe}/\text{H}]_{\text{LTE}} - 0.32(\pm 0.06), \\ \text{for } [\text{Fe}/\text{H}]_{\text{LTE}} < -2.0 \end{cases} \quad (9)$$

The two relations from these equations for $\Delta[\text{Fe}/\text{H}]$, as well as that derived in Ezzeddine et al. (2017), are shown in Figure 10, fit to

our test sample stars from Section 3 as well as the RPA sample. We find that even though the three relations agree within uncertainties (colored bands in Figure 10), they can, however, yield slightly different NLTE corrections depending on the metallicity range for which they were fit. For e.g., our relation derived using stars with $[\text{Fe}/\text{H}] < -2.0$ underestimates the NLTE $[\text{Fe}/\text{H}]$ correction as compared to Ezzeddine et al. (2017) by ~ 0.1 dex at $[\text{Fe}/\text{H}] = -2.0$, while using the relation derived with $[\text{Fe}/\text{H}] < -0.5$ can underestimate the NLTE correction up to 0.2 dex. This demonstrates that while these relations can provide useful first-order estimates of the NLTE corrections, a complete NLTE analysis (e.g., using LOTUS) is needed for precise estimation of the corrections, as the former can be dependent on the incomplete sample of stars or metallicity range.

Similarly, we derive ΔNLTE corrections for T_{eff} , $\log g$, and v_{mic} for our sample stars. Again, we define the NLTE correction for T_{eff} as $\Delta T_{\text{eff}} = T_{\text{eff}}(\text{NLTE}) - T_{\text{eff}}(\text{LTE})$, for $\log g$ as $\Delta \log g = \log g(\text{NLTE}) - \log g(\text{LTE})$, and for v_{mic} as $\Delta v_{\text{mic}} = v_{\text{mic}}(\text{NLTE}) - v_{\text{mic}}(\text{LTE})$. To best represent these corrections as a function of the other stellar parameters, we divide our sample into box plots grouped into different T_{eff} and $\log g$ bins, as a function of $[\text{Fe}/\text{H}]$ on the x-axis. The results are shown in Figure 11.

In what follows we discuss the NLTE corrections we obtained for each parameter as a function of the other parameters, namely T_{eff} , $\log g$ and $[\text{Fe}/\text{H}]$. We also compare our result to the theoretical NLTE stellar parameter corrections derived by Lind et al. (2012). We note, however, that our comparisons are affected by the fact that our analyzed stars do not cover exactly the same parameter space as theirs, and that our stellar parameters have been derived by LOTUS simultaneously, i.e., taking into account their inter-dependencies, as explained in details in Section 2, whereas Lind et al. (2012)

derived their Δ NLTE corrections for each parameter independently, by fixing all the others. As shown in Figure 11, we find that the T_{eff} derived in NLTE are generally higher than those in LTE for very metal-poor ($[\text{Fe}/\text{H}] < -2.5$) supergiants and giant stars ($\log g < 2.0$), with NLTE corrections up to 100 K, whereas lower T_{eff} are obtained in NLTE as compared to LTE as $\log g$ and $[\text{Fe}/\text{H}]$ increases. Lind et al. (2012), who derived their T_{eff} using both excitation and ionization equilibrium by fixing gravity and other stellar parameters in the process. Similarly, they also restrict their Fe I line transitions to certain cutoffs, choosing only lines with $\text{EP} > 3.5$ eV. They found that their ionization ΔT_{eff} yielded lower LTE T_{eff} as compared to NLTE (see their Figure 5), whereas their excitation ΔT_{eff} yielded negligible positive corrections for $T_{\text{eff}} < 4500$. More pronounced negative corrections were obtained for horizontal branches, supergiants, and extremely metal-poor stars, which are not covered in our sample stars. As noted above, our derived T_{eff} using LOTUS implement the contribution from both excitation and ionization equilibrium, by taking into account their T_{eff} - $\log g$ inter-dependencies. In that context, a thorough comparison of our ΔT_{eff} results to either excitation or ionization theoretical corrections derived by Lind et al. (2012) are not very useful, however, similar to their results we generally find that the NLTE corrections for the bulk of our stars are affected by less than 50 K (and up to 100 K) in the considered parameter range, which is within our derived uncertainties.

We also derive $\Delta \log g$ for our sample stars. As expected, the NLTE corrections for $\log g$ increase towards lower gravities, lower metallicities, and higher temperatures. On average, our corrections are $\sim +0.3 - 0.5$ for $[\text{Fe}/\text{H}] < -2.0$, $\sim +0.1 - 0.3$ for $-2.0 < [\text{Fe}/\text{H}] < -1.0$, for giants and supergiant stars with $\log g < 2.0$, with outliers reaching up to 1.0 dex. For stars with $\log g > 2.0$, the NLTE corrections can be up to

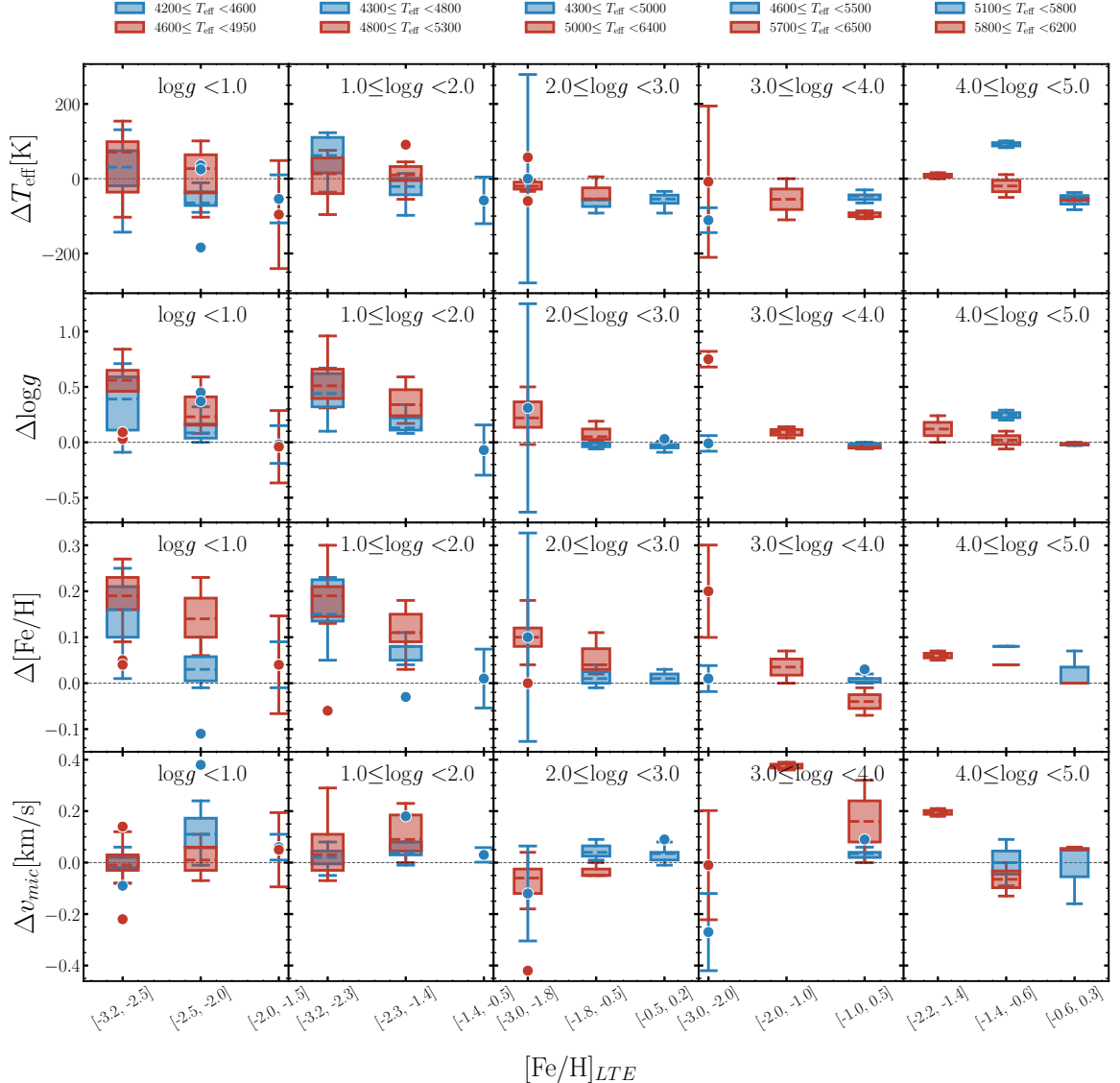


Figure 11. Box plots showing the NLTE corrections of stars considered in this work for stellar parameter T_{eff} , $\log g$, $[\text{Fe}/\text{H}]$, and v_{mic} as derived using **LOTUS**. Box plots are color-coded for two ranges of T_{eff} for each $\log g$ range, indicated at the top of each column. For intervals with only one star from our sample, boxes are replaced with dots and their error bars.

~0.3 depending on metallicities. These results broadly agree with the theoretical corrections derived in Lind et al. (2012). It can thus be concluded that LTE analyses can strongly underestimate the surface gravities of stars, particularly for warmer metal-poor giants, and should thus be reliably derived in NLTE for reliable consequent stellar population analyses.

Finally, the NLTE corrections for v_{mic} are generally small and are within 2.0 km s^{-1} from

those derived in LTE. The corrections are mainly positive for lower metallicity giants and supergiant stars, as in particular their Fe I lines are more strongly affected by NLTE, which leads to lower microturbulent velocities in LTE as compared to NLTE. Our results are generally consistent with the Δv_{mic} derived by Lind et al. (2012) from their theoretical models.

5. CAVEATS

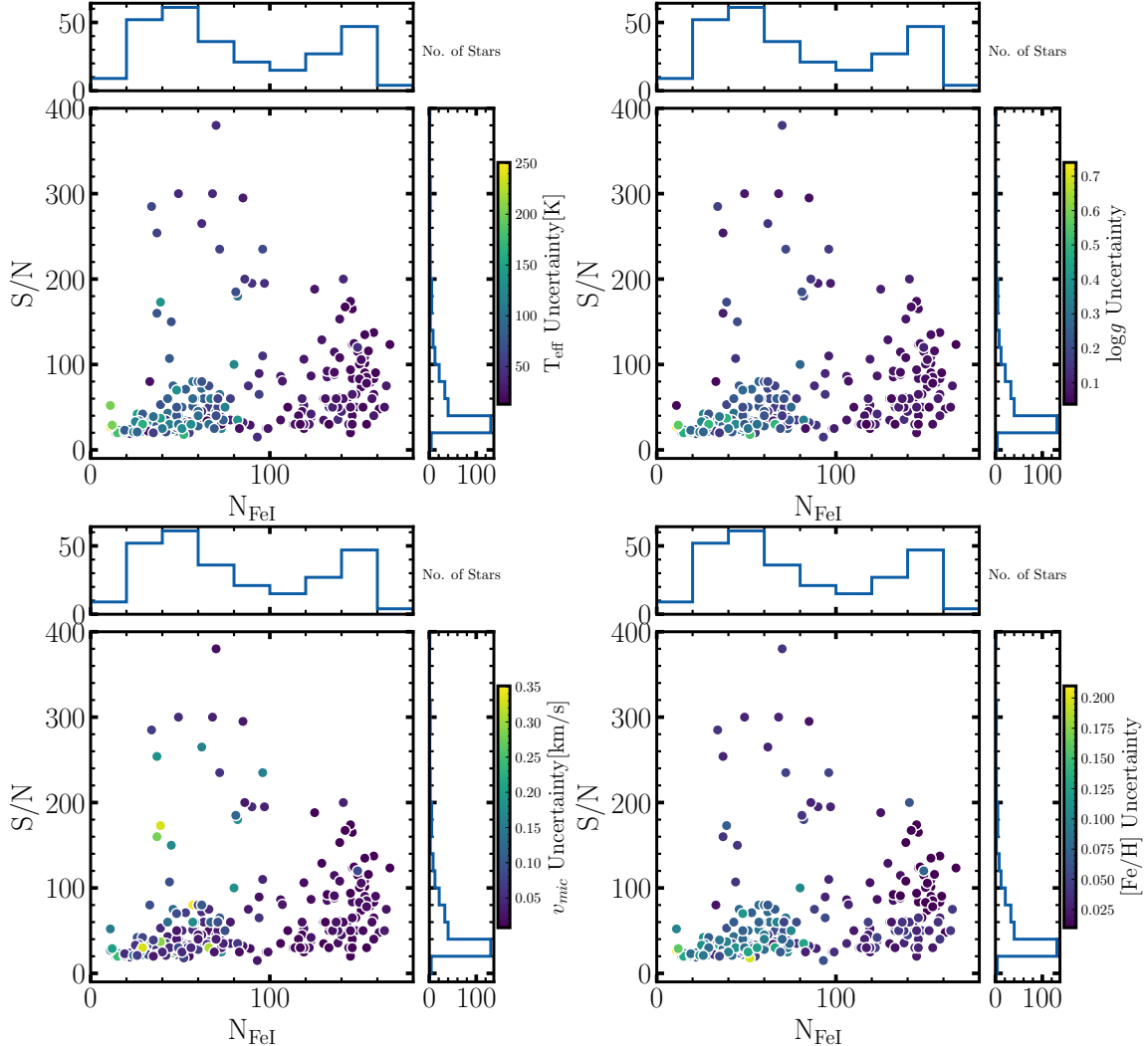


Figure 12. Derived stellar parameter uncertainties as a functions of the number of Fe I lines and S/N ratios in our sample of stars from Section 4, in addition to metal-poor stars with high S/N from [Ezzeddine et al. \(2020\)](#).

We have so far described and demonstrated that LOTUS can be used as a reliable tool to derive NLTE and LTE atmospheric stellar parameters. There are, however, some caveats that warrant pointing out which can affect the results, particularly for stars occupying certain parameter spaces in our grids.

EW Interpolation—A key component of LOTUS is its interpolation module that expresses the EW as a function of stellar parameters, using the generalized curve of growth (GCOG). As explained in Section 2.3.1, we conduct thorough tests to choose the best polynomial interpolator

for each spectral type. However, we find that some models are not adequate to reliably fit the GCOG, particularly for parameter regions where EW variations have smaller dependencies on stellar parameters. This is demonstrated in Figure 2, where the EW of the Fe I line at 4077 Å varies less strongly with v_{mic} at higher T_{eff} and lower $\log g$. Thus, the iron abundances derived from these interpolated models can deviate up to 0.5 dex in abundances from those computed directly from MULTI2.3 output (i.e., non interpolated EWs). Such large offsets are likely due to lower than optimal orders of polynomials cho-

sen for some spectral types in these parameter regions (see Section 2.3.1 for details), where the EW of those lines not being sensitive to the variation of atmospheric stellar parameters, or being too small (close to zero) at most atmospheric stellar parameters. We emphasize though, that the number of such lines is limited and should not impact the statistical properties of the interpolation performance for the lines considered in our linelist, as shown in Figure 3.

Number of Fe I lines and S/N ratios—The derived atmospheric stellar parameters could be affected by the number of Fe I and Fe II lines utilized in the parameter optimization in **LOTUS**. We, therefore, investigate the derived uncertainties of the stellar parameters using **LOTUS** as a function of the number of Fe I lines and the S/N ratio as shown in Figure 12. To demonstrate our results over a representative statistical sample of stars covering a wide range of S/N ratios, we use the full star sample from Section 4, supplemented by metal-poor stars from Ezzeddine et al. (2020) which cover higher S/N values ($S/N > 100$) than those in Hansen et al. (2018). We can see in Figure 12 that the uncertainties derived for each stellar parameter as a function of the number of Fe I and S/N ratio decrease as a function of increasing the number of Fe I and increasing the S/N ratio. For stars with $N_{\text{lines}} > 100$ or stars with $N_{\text{lines}} < 100$ and $S/N > 100$, the uncertainty are $< 50 \text{ K}$ for T_{eff} , $< 0.1 \text{ dex}$ for $\log g$, $< 0.05 \text{ dex}$ for $[\text{Fe}/\text{H}]$ and $< 0.02 \text{ km s}^{-1}$ for v_{mic} . For stars with $N_{\text{lines}} < 100$ and $S/N < 60$, however, the uncertainties can reach up to 200 K for T_{eff} , 0.5 dex for $\log g$, 0.3 dex for $[\text{Fe}/\text{H}]$ and 0.2 km s^{-1} for v_{mic} . It is notable to mention, though, that higher uncertainties are more strongly correlated to lower S/N (< 40). We thus recommend that users try to utilize "good-quality" EW measurements for their Fe I (and Fe II) lines to obtain reliable results and smaller uncertainty derivation in **LOTUS**. This is particularly useful if the

number of measured EW lines for a star is too small (< 100). Additionally, as the number of Fe II lines usually detected in cool FGK stellar spectra can be smaller than the number of Fe I lines (on the order of 5-25 lines, depending on the $[\text{Fe}/\text{H}]$ of the star), we moreover recommend that users try to maximize the number of Fe II EW line measurements in the stars, if possible, to increase the precision of the parameter determination. In future work, we plan to test **LOTUS** on a sample of low resolution spectroscopic observations (as compared to high-resolution data for the same stars) to accurately quantify the effects of the spectral resolution on the results of the stellar parameters derived by **LOTUS**.

K-type stars—The atmospheric stellar parameters, particularly $\log g$, derived for K-type stars using **LOTUS** can have larger uncertainties than those derived for other spectral types. Tsantaki et al. (2019) noted that $\log g$ determined for K-type stars using ionization balance between Fe I and Fe II lines are underestimated depending on the choice of Fe II lines used in the optimization. We investigate this effect on our GES-K2 sample, in which most of the stars are K-type giants or sub-giants. We find that both our NLTE and LTE results can indeed overestimate the surface gravities up to 0.1 dex as compared to asteroseismic values, depending on the selection of Fe II lines.

3D models—Since our atmospheric stellar models are limited to 1D, our determined iron abundances might suffer from 3D effects due to atmospheric inhomogeneities, horizontal radiation transfer, as well as the differences in the mean temperature stratification Amarsi et al. (2016) between 1D and 3D models. The latter can lead to underestimated abundances derived from Fe I and Fe II lines, on average up to 0.1 dex in 1D, NLTE as compared with Fe abundances derived using 3D, NLTE. Such effects are, however, more strongly pronounced for Fe II lines

than Fe I as explained in Amarsi et al. (2016). We find that adding a 0.1 dex correction for our 1D, NLTE [Fe/H] for HD122563 brings it closer to the 3D, NLTE [Fe/H] derived in (Amarsi et al. 2016).

On the other hand, we find that a difference of 0.2 dex as compared to Amarsi et al. (2016) is still present when adding the same [Fe/H] correction for HD140283. This can be explained by the stellar parameter differences adopted in both studies, as well as the difference between linelists. However, as noted in Amarsi et al. (2016) and Amarsi et al. (2022), 3D corrections can nevertheless be smaller than the NLTE corrections determined for low metallicity evolved stars. Therefore, including 1D, NLTE corrections in the determination of Fe I and Fe II lines can significantly improve the derived stellar parameters as compared to 1D, LTE.

6. SUMMARY & CONCLUSIONS

We present the open-source code, **LOTUS**, developed to automatically derive fast and precise atmospheric stellar parameters (T_{eff} , $\log g$, [Fe/H] and v_{mic}) of stars in 1D, LTE, and 1D, NLTE using Fe I and Fe II equivalent width measurement from stellar spectra.

LOTUS implements a generalized curve of growth (GCOG) interpolation to derive abundances from a pre-computed grid of theoretical NLTE EW in a high-resolution and dense spectral parameter space. The GCOG takes into account the EW dependencies on stellar atmospheric parameters. A global differential evolution optimization algorithm, tailored to the spectral type of the star, is then used to derive the fundamental stellar parameters. In addition, **LOTUS** can be used to estimate precise uncertainties for each stellar parameter using a well-tested Markov Chain Monte Carlo (MCMC) algorithm.

We tested our code on several benchmark stars and stellar samples with reliable non-spectroscopic (from asteroseismic, photomet-

ric, and interferometric observations) measurements for a wide range of parameter space typical for FGK stars. We find that our NLTE-derived stellar parameters for T_{eff} and $\log g$ are within 30 K and 0.1 dex for benchmark stars including the metal-poor standard stars, HD140283 and HD122563, as well as Arcturus. We also test **LOTUS** on a large sample of *Gaia*-ESO (GES) dwarf stars from Hawkins et al. (2016) and GES-K2 with asteroseismic gravities from K2, as well as stars with CHARA interferometric observations. Similarly, we find that **LOTUS** performs very well in reproducing the non-spectroscopic T_{eff} and $\log g$ on average within < 20 K and < 0.1 dex in NLTE, as compared to ~ 70 K and ~ 0.2 dex in LTE.

Moreover, we apply **LOTUS** on a large sample of metal-poor stars from the R-Process Alliance (RPA, Hansen et al. 2018). We use the RPA sample as well as the test sample stars to derive NLTE stellar parameter corrections for our stars and review the $\Delta[\text{Fe}/\text{H}]$ versus [Fe/H](LTE) relation derived in Ezzeddine et al. (2017). We find that our NLTE corrections agree with theoretical corrections predicted by Lind et al. (2012), where general trends of corrections were found to increasing toward metal-poor evolved stars, as expected.

We test **LOTUS** thoroughly for its performance for different spectral types and parameter space. We find that despite some caveats discussed in Section 5, **LOTUS** can overall be reliably used to provide fast and accurate NLTE derivation for a wide range of stellar parameters, especially metal-poor giants which can be strongly affected by deviations from LTE. We thus strongly recommend that the community use it to apply for the spectroscopic analyses of stars and stellar populations.

We provide open community access to **LOTUS**, as well as the pre-computed interpolated LTE and NLTE EW grids available on Github 

with documentation and working examples on Readthedocs [\[E\]](#).

ACKNOWLEDGMENTS

We thank the anonymous referee for their useful comments that helped improved the manuscript. R.E. acknowledges support from JINA-CEE (Joint Institute for Nuclear Astrophysics - Center for the Evolution of the Elements), funded by the NSF under Grant No. PHY-1430152. Y.L. and R.E. acknowledge support from NSF grant AST-2206263. The authors acknowledge the University of Florida Research Computing for providing computational resources and support that have contributed to the research results reported in this publication.

URL: [UFRC](#).

Software: astropy (Astropy Collaboration et al. 2013, 2018), numpy (van der Walt et al. 2011; Harris et al. 2020), pandas (pandas development team 2020), scikit-learn (Buitinck et al. 2013), scipy (Virtanen et al. 2020), sympy (Meurer et al. 2017), matplotlib (Hunter 2007), h5py (Collette 2013), PyMC3 (Salvatier et al. 2016), theano (Team et al. 2016), corner (Foreman-Mackey 2016), numdifftools (Brodtkorb & D’Errico 2015)

APPENDIX

A. LINELIST OF Fe I AND Fe II IN LOTUS

Table 2. Fe I and Fe II linelist selected for LOTUS (see Section 2.1.4 for details)

Species	$\lambda(\text{\AA})$	$E_{low}(\text{ev})$	loggf
Fe I	3440.61	0.00	-0.67
Fe I	3440.99	0.05	-0.96
Fe I	3447.28	2.20	-1.02
Fe I	3450.33	2.22	-0.90
Fe I	3451.91	2.22	-1.00
Fe I	3476.70	0.12	-1.51
Fe I	3490.57	0.05	-1.10
Fe I	3497.84	0.11	-1.55
Fe I	3540.12	2.87	-0.71
Fe I	3565.38	0.96	-0.13
Fe I	3608.86	1.01	-0.10
Fe I	3618.77	0.99	-0.00
Fe I	3647.84	0.92	-0.19
Fe I	3689.46	2.94	-0.17
Fe I	3719.93	0.00	-0.43
Fe I	3727.62	0.96	-0.63
Fe I	3742.62	2.94	-0.81
Fe I	3758.23	0.96	-0.03
Fe I	3763.79	0.99	-0.24
Fe I	3765.54	3.24	0.48
Fe I	3786.68	1.01	-2.22
Fe I	3787.88	1.01	-0.86
Fe I	3805.34	3.30	0.31
Fe I	3808.73	2.56	-1.17
Fe I	3815.84	1.48	0.23
Fe I	3820.43	0.86	0.12
Fe I	3825.88	0.91	-0.04
Fe I	3827.82	1.56	0.06
Fe I	3840.44	0.99	-0.51
Fe I	3841.05	1.61	-0.04
Fe I	3849.97	1.01	-0.87
Fe I	3856.37	0.05	-1.29

Table 2 (continued)

Species	$\lambda(\text{\AA})$	$E_{low}(\text{ev})$	loggf
Fe I	3865.52	1.01	-0.98
Fe I	3878.02	0.96	-0.91
Fe I	3895.66	0.11	-1.67
Fe I	3899.71	0.09	-1.53
Fe I	3902.95	1.56	-0.47
Fe I	3920.26	0.12	-1.75
Fe I	3922.91	0.05	-1.65
Fe I	3949.95	2.18	-1.25
Fe I	3977.74	2.20	-1.12
Fe I	4005.24	1.56	-0.61
Fe I	4045.81	1.49	0.28
Fe I	4058.22	3.21	-1.18
Fe I	4063.59	1.56	0.06
Fe I	4067.98	3.21	-0.53
Fe I	4070.77	3.24	-0.87
Fe I	4071.74	1.61	-0.02
Fe I	4114.44	2.83	-1.30
Fe I	4132.06	1.61	-0.68
Fe I	4134.68	2.83	-0.65
Fe I	4143.87	1.56	-0.51
Fe I	4147.67	1.49	-2.10
Fe I	4150.25	3.43	-1.19
Fe I	4154.50	2.83	-0.69
Fe I	4156.80	2.83	-0.81
Fe I	4157.78	3.42	-0.40
Fe I	4158.79	3.43	-0.70
Fe I	4174.91	0.91	-2.97
Fe I	4175.64	2.85	-0.83
Fe I	4181.76	2.83	-0.37
Fe I	4182.38	3.02	-1.18
Fe I	4184.89	2.83	-0.87
Fe I	4187.04	2.45	-0.56
Fe I	4187.80	2.42	-0.55
Fe I	4191.43	2.47	-0.67

Table 2 *continued***Table 2** *continued*

Table 2 (*continued*)

Species	$\lambda(\text{\AA})$	$E_{low}(\text{ev})$	loggf
Fe I	4195.33	3.33	-0.49
Fe I	4199.10	3.05	0.16
Fe I	4202.03	1.49	-0.71
Fe I	4216.18	0.00	-3.36
Fe I	4217.55	3.43	-0.48
Fe I	4222.21	2.45	-0.97
Fe I	4227.43	3.33	0.27
Fe I	4233.60	2.48	-0.60
Fe I	4238.81	3.40	-0.23
Fe I	4250.12	2.47	-0.41
Fe I	4250.79	1.56	-0.71
Fe I	4260.47	2.40	0.08
Fe I	4271.15	2.45	-0.35
Fe I	4271.76	1.49	-0.16
Fe I	4282.40	2.18	-0.78
Fe I	4325.76	1.61	0.01
Fe I	4352.73	2.22	-1.29
Fe I	4375.93	0.00	-3.03
Fe I	4388.41	3.60	-0.68
Fe I	4404.75	1.56	-0.14
Fe I	4415.12	1.61	-0.62
Fe I	4427.31	0.05	-3.04
Fe I	4430.61	2.22	-1.66
Fe I	4432.57	3.57	-1.58
Fe I	4442.34	2.20	-1.25
Fe I	4443.19	2.86	-1.04
Fe I	4447.72	2.22	-1.36
Fe I	4461.65	0.09	-3.21
Fe I	4466.55	2.83	-0.60
Fe I	4484.22	3.60	-0.64
Fe I	4489.74	0.12	-3.97
Fe I	4494.56	2.20	-1.14
Fe I	4514.18	3.05	-1.96
Fe I	4531.15	1.48	-2.16
Fe I	4547.85	3.55	-0.82
Fe I	4574.22	3.21	-2.35
Fe I	4592.65	1.56	-2.45
Fe I	4595.36	3.30	-1.76

Table 2 (*continued*)

Species	$\lambda(\text{\AA})$	$E_{low}(\text{ev})$	loggf
Fe I	4602.00	1.61	-3.15
Fe I	4602.94	1.49	-2.22
Fe I	4607.65	3.27	-1.33
Fe I	4619.29	3.60	-1.06
Fe I	4630.12	2.28	-2.58
Fe I	4637.50	3.28	-1.29
Fe I	4643.46	3.65	-1.15
Fe I	4647.43	2.95	-1.35
Fe I	4661.97	2.99	-2.50
Fe I	4668.13	3.27	-1.08
Fe I	4704.95	3.69	-1.32
Fe I	4733.59	1.49	-2.99
Fe I	4736.77	3.21	-0.67
Fe I	4786.81	3.02	-1.61
Fe I	4787.83	3.00	-2.62
Fe I	4788.76	3.24	-1.763
Fe I	4789.65	3.55	-0.96
Fe I	4793.96	3.05	-3.43
Fe I	4794.35	2.42	-3.95
Fe I	4800.65	4.14	-1.03
Fe I	4802.88	3.64	-1.51
Fe I	4807.71	3.37	-2.15
Fe I	4808.15	3.25	-2.69
Fe I	4869.46	3.55	-2.42
Fe I	4871.32	2.87	-0.34
Fe I	4872.14	2.88	-0.57
Fe I	4873.75	3.30	-2.96
Fe I	4875.88	3.33	-1.90
Fe I	4877.60	3.00	-3.05
Fe I	4882.14	3.42	-1.48
Fe I	4885.43	3.88	-0.97
Fe I	4890.76	2.88	-0.38
Fe I	4891.49	2.85	-0.11
Fe I	4896.44	3.88	-1.89
Fe I	4903.31	2.88	-0.89
Fe I	4905.13	3.93	-1.73
Fe I	4907.73	3.43	-1.70
Fe I	4910.02	3.40	-1.28

Table 2 *continued***Table 2** *continued*

Table 2 (*continued*)

Species	$\lambda(\text{\AA})$	$E_{low}(\text{ev})$	loggf
Fe I	4911.78	3.93	-1.75
Fe I	4918.99	2.86	-0.34
Fe I	4920.50	2.83	0.07
Fe I	4924.77	2.28	-2.11
Fe I	4938.81	2.88	-1.08
Fe I	4939.69	0.86	-3.34
Fe I	4946.39	3.37	-1.11
Fe I	4950.11	3.42	-1.49
Fe I	4962.57	4.18	-1.18
Fe I	4966.09	3.33	-0.79
Fe I	4969.92	4.22	-0.71
Fe I	4985.55	2.87	-1.33
Fe I	4992.79	4.26	-2.35
Fe I	4994.13	0.92	-3.08
Fe I	4999.11	4.19	-1.64
Fe I	5001.86	3.88	-0.01
Fe I	5002.79	3.40	-1.46
Fe I	5005.71	3.88	-0.12
Fe I	5006.12	2.83	-0.61
Fe I	5012.69	4.28	-1.69
Fe I	5014.94	3.94	-0.18
Fe I	5022.24	3.98	-0.33
Fe I	5023.19	4.28	-1.50
Fe I	5028.13	3.57	-1.02
Fe I	5039.25	3.37	-1.52
Fe I	5044.21	2.85	-2.02
Fe I	5048.44	3.96	-1.00
Fe I	5049.82	2.28	-1.35
Fe I	5051.63	0.92	-2.80
Fe I	5054.64	3.64	-1.92
Fe I	5058.50	3.64	-2.83
Fe I	5060.08	0.00	-5.43
Fe I	5068.77	2.94	-1.04
Fe I	5079.22	2.20	-2.07
Fe I	5079.74	0.99	-3.22
Fe I	5083.34	0.96	-2.96
Fe I	5088.15	4.15	-1.68
Fe I	5107.45	0.99	-3.09

Table 2 (*continued*)

Species	$\lambda(\text{\AA})$	$E_{low}(\text{ev})$	loggf
Fe I	5107.64	1.56	-2.36
Fe I	5109.65	4.30	-0.98
Fe I	5115.78	3.57	-2.64
Fe I	5123.72	1.01	-3.07
Fe I	5127.36	0.92	-3.31
Fe I	5131.47	2.22	-2.52
Fe I	5133.69	4.18	0.36
Fe I	5141.74	2.42	-2.24
Fe I	5150.84	0.99	-3.04
Fe I	5151.91	1.01	-3.32
Fe I	5166.28	0.00	-4.20
Fe I	5171.60	1.49	-1.79
Fe I	5191.45	3.04	-0.55
Fe I	5192.34	3.00	-0.42
Fe I	5194.94	1.56	-2.09
Fe I	5197.94	4.30	-1.54
Fe I	5198.71	2.22	-2.13
Fe I	5202.34	2.18	-1.84
Fe I	5215.18	3.27	-0.86
Fe I	5216.27	1.61	-2.15
Fe I	5217.39	3.21	-1.07
Fe I	5223.18	3.63	-1.78
Fe I	5225.53	0.11	-4.79
Fe I	5228.38	4.22	-1.19
Fe I	5232.94	2.94	-0.06
Fe I	5242.49	3.63	-0.97
Fe I	5243.78	4.26	-1.05
Fe I	5247.05	0.09	-4.95
Fe I	5250.21	0.12	-4.93
Fe I	5250.65	2.20	-2.18
Fe I	5253.02	2.28	-3.84
Fe I	5253.46	3.28	-1.58
Fe I	5262.88	3.25	-2.56
Fe I	5263.31	3.27	-0.87
Fe I	5266.56	3.00	-0.39
Fe I	5281.79	3.04	-0.83
Fe I	5283.62	3.24	-0.52
Fe I	5285.13	4.43	-1.66

Table 2 *continued***Table 2** *continued*

Table 2 (*continued*)

Species	$\lambda(\text{\AA})$	$E_{low}(\text{ev})$	loggf
Fe I	5288.52	3.69	-1.49
Fe I	5293.96	4.14	-1.77
Fe I	5294.55	3.64	-2.76
Fe I	5295.31	4.42	-1.59
Fe I	5300.40	4.59	-1.65
Fe I	5302.30	3.28	-0.74
Fe I	5307.36	1.61	-2.99
Fe I	5321.11	4.43	-1.09
Fe I	5322.04	2.28	-2.80
Fe I	5324.18	3.21	-0.11
Fe I	5332.90	1.56	-2.78
Fe I	5339.93	3.27	-0.63
Fe I	5341.02	1.61	-1.95
Fe I	5364.87	4.45	0.23
Fe I	5365.40	3.57	-1.02
Fe I	5367.47	4.42	0.44
Fe I	5369.96	4.37	0.54
Fe I	5371.49	0.96	-1.64
Fe I	5373.71	4.47	-0.71
Fe I	5379.57	3.69	-1.42
Fe I	5383.37	4.31	0.65
Fe I	5386.33	4.15	-1.67
Fe I	5389.48	4.42	-0.41
Fe I	5395.22	4.45	-2.07
Fe I	5397.13	0.92	-1.99
Fe I	5398.28	4.45	-0.63
Fe I	5405.77	0.99	-1.85
Fe I	5410.91	4.47	0.4
Fe I	5412.78	4.43	-1.72
Fe I	5415.20	4.39	0.64
Fe I	5417.03	4.42	-1.58
Fe I	5424.07	4.32	0.52
Fe I	5429.70	0.96	-1.88
Fe I	5434.52	1.01	-2.12
Fe I	5436.59	2.28	-2.96
Fe I	5441.34	4.31	-1.63
Fe I	5445.04	4.39	-0.02
Fe I	5461.55	4.45	-1.8

Table 2 (*continued*)

Species	$\lambda(\text{\AA})$	$E_{low}(\text{ev})$	loggf
Fe I	5464.28	4.14	-1.40
Fe I	5466.40	4.37	-0.63
Fe I	5470.09	4.45	-1.71
Fe I	5473.90	4.15	-0.72
Fe I	5483.10	4.15	-1.39
Fe I	5487.15	4.42	-1.43
Fe I	5491.83	4.19	-2.19
Fe I	5493.50	4.10	-1.48
Fe I	5494.46	4.08	-1.99
Fe I	5497.52	1.01	-2.85
Fe I	5501.47	0.96	-3.05
Fe I	5506.78	0.99	-2.80
Fe I	5522.45	4.21	-1.45
Fe I	5525.54	4.23	-1.08
Fe I	5536.58	2.83	-3.71
Fe I	5539.28	3.64	-2.56
Fe I	5543.94	4.22	-1.04
Fe I	5546.51	4.37	-1.21
Fe I	5552.69	4.95	-1.89
Fe I	5554.90	4.55	-0.27
Fe I	5560.21	4.43	-1.09
Fe I	5563.60	4.19	-0.75
Fe I	5569.62	3.42	-0.52
Fe I	5576.09	3.43	-0.90
Fe I	5586.76	3.37	-0.11
Fe I	5587.57	4.14	-1.75
Fe I	5618.63	4.21	-1.25
Fe I	5619.60	4.39	-1.60
Fe I	5624.02	4.39	-1.38
Fe I	5624.54	3.42	-0.76
Fe I	5633.95	4.99	-0.23
Fe I	5635.82	4.26	-1.79
Fe I	5636.70	3.64	-2.51
Fe I	5638.26	4.22	-0.72
Fe I	5641.43	4.26	-1.08
Fe I	5649.99	5.10	-0.82
Fe I	5651.47	4.47	-1.90
Fe I	5652.32	4.26	-1.85

Table 2 *continued***Table 2** *continued*

Table 2 (*continued*)

Species	$\lambda(\text{\AA})$	$E_{low}(\text{ev})$	loggf
Fe I	5653.87	4.39	-1.54
Fe I	5655.18	5.06	-0.60
Fe I	5661.35	4.28	-1.76
Fe I	5662.52	4.18	-0.41
Fe I	5667.52	4.18	-1.58
Fe I	5679.02	4.65	-0.82
Fe I	5686.53	4.55	-0.45
Fe I	5691.50	4.30	-1.45
Fe I	5696.09	4.55	-1.72
Fe I	5698.02	3.64	-2.58
Fe I	5701.54	2.56	-2.22
Fe I	5705.46	4.30	-1.35
Fe I	5731.76	4.26	-1.20
Fe I	5732.30	4.99	-1.46
Fe I	5741.85	4.26	-1.67
Fe I	5742.96	4.18	-2.41
Fe I	5753.12	4.26	-0.62
Fe I	5760.34	3.64	-2.39
Fe I	5775.08	4.22	-1.08
Fe I	5778.45	2.59	-3.43
Fe I	5784.66	3.40	-2.55
Fe I	5816.37	4.55	-0.60
Fe I	5835.10	4.26	-2.27
Fe I	5837.70	4.29	-2.24
Fe I	5838.37	3.94	-2.24
Fe I	5849.68	3.69	-2.89
Fe I	5853.15	1.49	-5.18
Fe I	5855.08	4.61	-1.48
Fe I	5858.78	4.22	-2.16
Fe I	5883.82	3.96	-1.26
Fe I	5902.47	4.59	-1.71
Fe I	5905.67	4.65	-0.69
Fe I	5916.25	2.45	-2.99
Fe I	5927.79	4.65	-0.99
Fe I	5929.68	4.55	-1.31
Fe I	5930.18	4.65	-0.23
Fe I	5934.65	3.93	-1.07
Fe I	5940.99	4.18	-2.05

Table 2 (*continued*)

Species	$\lambda(\text{\AA})$	$E_{low}(\text{ev})$	loggf
Fe I	5956.69	0.86	-4.60
Fe I	6003.01	3.88	-1.10
Fe I	6008.56	3.88	-0.98
Fe I	6012.21	2.22	-4.04
Fe I	6024.06	4.55	-0.12
Fe I	6027.05	4.08	-1.09
Fe I	6056.00	4.73	-0.32
Fe I	6065.48	2.61	-1.53
Fe I	6079.01	4.65	-1.02
Fe I	6082.71	2.22	-3.58
Fe I	6093.64	4.61	-1.40
Fe I	6094.37	4.65	-1.84
Fe I	6096.66	3.98	-1.83
Fe I	6120.25	0.91	-5.97
Fe I	6127.91	4.14	-1.40
Fe I	6136.61	2.45	-1.40
Fe I	6136.99	2.20	-2.95
Fe I	6137.69	2.59	-1.40
Fe I	6151.62	2.18	-3.30
Fe I	6165.36	4.14	-1.47
Fe I	6173.33	2.22	-2.88
Fe I	6187.99	3.94	-1.62
Fe I	6191.56	2.43	-1.42
Fe I	6200.31	2.61	-2.43
Fe I	6213.43	2.22	-2.48
Fe I	6219.28	2.20	-2.43
Fe I	6226.73	3.88	-2.12
Fe I	6229.23	2.85	-2.81
Fe I	6230.72	2.56	-1.28
Fe I	6232.64	3.65	-1.24
Fe I	6240.65	2.22	-3.17
Fe I	6246.32	3.60	-0.77
Fe I	6252.56	2.40	-1.69
Fe I	6265.13	2.18	-2.55
Fe I	6270.22	2.86	-2.47
Fe I	6271.28	3.33	-2.70
Fe I	6297.79	2.22	-2.74
Fe I	6301.50	3.65	-0.71

Table 2 *continued***Table 2** *continued*

Table 2 (*continued*)

Species	$\lambda(\text{\AA})$	$E_{low}(\text{ev})$	loggf
Fe I	6315.81	4.08	-1.63
Fe I	6322.69	2.59	-2.43
Fe I	6330.85	4.73	-1.64
Fe I	6335.33	2.20	-2.18
Fe I	6336.82	3.69	-0.85
Fe I	6338.88	4.80	-0.96
Fe I	6344.15	2.43	-2.92
Fe I	6355.03	2.84	-2.29
Fe I	6364.36	4.80	-1.33
Fe I	6380.74	4.19	-1.38
Fe I	6393.60	2.43	-1.58
Fe I	6400.32	0.91	-4.32
Fe I	6408.02	3.69	-0.99
Fe I	6411.65	3.65	-0.59
Fe I	6421.35	2.28	-2.03
Fe I	6430.85	2.18	-2.01
Fe I	6475.62	2.56	-2.94
Fe I	6481.87	2.28	-2.98
Fe I	6494.98	2.40	-1.27
Fe I	6496.47	4.80	-0.53
Fe I	6498.94	0.96	-4.69
Fe I	6518.37	2.83	-2.44
Fe I	6533.93	4.56	-1.36
Fe I	6546.24	2.76	-1.54
Fe I	6569.21	4.73	-0.38
Fe I	6574.23	0.99	-5.00
Fe I	6592.91	2.73	-1.47
Fe I	6593.87	2.43	-2.42
Fe I	6597.56	4.80	-0.97
Fe I	6609.11	2.56	-2.69
Fe I	6627.54	4.55	-1.59
Fe I	6648.08	1.01	-5.92
Fe I	6677.99	2.69	-1.42
Fe I	6699.14	4.59	-2.10
Fe I	6703.57	2.76	-3.06
Fe I	6713.74	4.80	-1.50
Fe I	6733.15	4.64	-1.15
Fe I	6739.52	1.56	-4.79

Table 2 (*continued*)

Species	$\lambda(\text{\AA})$	$E_{low}(\text{ev})$	loggf
Fe I	6750.15	2.42	-2.62
Fe I	6752.71	4.64	-1.20
Fe I	6786.86	4.19	-1.97
Fe I	6804.27	4.58	-1.81
Fe I	6806.84	2.73	-2.13
Fe I	6810.26	4.61	-0.99
Fe I	6820.37	4.64	-1.22
Fe I	6843.66	4.55	-0.73
Fe I	6855.16	4.56	-0.49
Fe I	6858.15	4.61	-0.90
Fe I	6978.85	2.48	-2.50
Fe I	7495.07	4.22	-0.10
Fe I	7511.02	4.18	0.12
Fe I	7568.90	4.28	-0.88
Fe I	8220.38	4.32	0.30
Fe II	4173.45	2.58	-2.38
Fe II	4178.86	2.58	-2.51
Fe II	4233.16	2.58	-2.02
Fe II	4303.17	2.70	-2.52
Fe II	4385.38	2.78	-2.64
Fe II	4416.82	2.78	-2.57
Fe II	4491.40	2.86	-2.71
Fe II	4508.28	2.86	-2.42
Fe II	4515.34	2.84	-2.60
Fe II	4522.63	2.84	-2.29
Fe II	4549.47	2.83	-1.92
Fe II	4555.89	2.83	-2.40
Fe II	4576.33	2.84	-2.95
Fe II	4583.83	2.81	-1.94
Fe II	4620.51	2.83	-3.21
Fe II	4923.93	2.89	-1.26
Fe II	4993.35	2.81	-3.68
Fe II	5197.57	3.23	-2.22
Fe II	5234.63	3.22	-2.18
Fe II	5256.93	2.89	-4.18
Fe II	5264.80	3.23	-3.13
Fe II	5276.00	3.20	-2.01
Fe II	5316.61	3.15	-1.87

Table 2 *continued***Table 2** *continued*

Table 2 (*continued*)

Species	$\lambda(\text{\AA})$	$E_{low}(\text{ev})$	loggf				
Fe II	5316.78	3.22	-2.74	Fe II	6149.24	3.89	-2.84
Fe II	5325.55	3.22	-3.16	Fe II	6247.56	3.89	-2.44
Fe II	5414.07	3.22	-3.58	Fe II	6369.46	2.89	-4.11
Fe II	5425.25	3.20	-3.22	Fe II	6432.68	2.89	-3.57
Fe II	5534.84	3.25	-2.80	Fe II	6456.38	3.90	-2.19
Fe II	5991.37	3.15	-3.65				
Fe II	6084.10	3.20	-3.88				
Fe II	6113.32	3.22	-4.23				

B. DERIVED STELLAR PARAMETERS OF THE TARGET STARS IN THIS WORK

Table 3. Derived Stellar Atmospheric Parameters of the Target Stars

Star Name	T_{eff} (K)	LTE			NLTE									
		$\log g$ (cgs)	[Fe/H] (dex)	v_{mic} (km s $^{-1}$)	$N_{\text{Fe I}}$ (ev)	$N_{\text{Fe I}}$ cutoff (ev)	$\chi_{\text{Fe I}}$ cutoff (ev)	T_{eff} (K)	$\log g$ (cgs)	[Fe/H] (dex)	v_{mic} (km s $^{-1}$)	$N_{\text{Fe I}}$	$N_{\text{Fe II}}$	$\chi_{\text{Fe I}}$ cutoff (ev)
HD122563	4528 \pm 42	0.66 \pm 0.12	-2.98 \pm 0.03	1.84 \pm 0.03	72	20	2.7	4620 \pm 59	1.21 \pm 0.19	-2.76 \pm 0.05	1.89 \pm 0.06	72	20	2.7
HD140283	5689 \pm 59	3.29 \pm 0.17	-2.72 \pm 0.04	2.09 \pm 0.14	96	15	2.0	5681 \pm 67	3.58 \pm 0.16	-2.64 \pm 0.05	2.17 \pm 0.16	96	15	2.0
Arcturus	4364 \pm 47	1.68 \pm 0.17	-0.64 \pm 0.05	1.76 \pm 0.02	70	8	0.0	4306 \pm 41	1.61 \pm 0.15	-0.63 \pm 0.04	1.79 \pm 0.02	70	8	0.0
GES Metal-Poor Stars (Hawkins et al. 2016)														
HD102200	6167 \pm 52	3.98 \pm 0.09	-1.26 \pm 0.02	0.62 \pm 0.09	33	4	2.5	6057 \pm 75	4.02 \pm 0.09	-1.26 \pm 0.04	0.98 \pm 0.28	37	4	2.5
HD106038	6108 \pm 51	4.05 \pm 0.07	-1.42 \pm 0.02	0.59 \pm 0.07	35	5	2.5	6124 \pm 60	4.29 \pm 0.08	-1.35 \pm 0.03	0.8 \pm 0.18	37	5	2.5
HD175305	5113 \pm 84	2.51 \pm 0.25	-1.47 \pm 0.05	1.61 \pm 0.2	45	6	2.5	5059 \pm 70	2.56 \pm 0.2	-1.43 \pm 0.04	1.61 \pm 0.17	45	6	2.5
HD201891	6036 \pm 86	4.23 \pm 0.15	-1.04 \pm 0.04	0.63 \pm 0.09	44	5	2.5	6047 \pm 81	4.33 \pm 0.14	-1.0 \pm 0.04	0.63 \pm 0.09	44	5	2.5
HD298986	6182 \pm 64	3.99 \pm 0.1	-1.42 \pm 0.03	0.61 \pm 0.08	37	5	2.5	6182 \pm 137	4.13 \pm 0.19	-1.35 \pm 0.07	1.0 \pm 0.33	39	5	2.5
CHARA Interferometry Stars (Karovcova et al. 2020, 2021a,b)														
HD131156	5538 \pm 46	4.55 \pm 0.1	-0.2 \pm 0.03	0.99 \pm 0.05	90	9	0.0	5501 \pm 47	4.53 \pm 0.1	-0.2 \pm 0.03	1.04 \pm 0.05	90	9	0.0
HD146233	5845 \pm 38	4.39 \pm 0.08	0.04 \pm 0.02	0.91 \pm 0.04	68	6	0.0	5788 \pm 39	4.37 \pm 0.08	0.04 \pm 0.03	0.96 \pm 0.04	68	6	0.0
HD186408	5842 \pm 46	4.33 \pm 0.1	0.03 \pm 0.03	1.1 \pm 0.03	96	11	0.0	5783 \pm 49	4.31 \pm 0.09	0.03 \pm 0.03	1.15 \pm 0.04	96	11	0.0
HD186427	5819 \pm 42	4.41 \pm 0.08	0.03 \pm 0.03	0.99 \pm 0.04	97	11	0.0	5771 \pm 45	4.41 \pm 0.09	0.03 \pm 0.03	1.05 \pm 0.04	97	11	0.0
HD190360	5538 \pm 33	4.37 \pm 0.06	0.13 \pm 0.02	0.8 \pm 0.05	49	9	0.0	5485 \pm 40	4.34 \pm 0.08	0.13 \pm 0.03	0.85 \pm 0.05	49	9	0.0
HD161797	5619 \pm 41	4.01 \pm 0.08	0.23 \pm 0.02	1.09 \pm 0.03	88	11	0.0	5536 \pm 30	3.99 \pm 0.06	0.3 \pm 0.02	0.93 \pm 0.03	85	11	0.0
HD207978	6493 \pm 24	3.99 \pm 0.05	-0.54 \pm 0.01	1.31 \pm 0.18	63	8	1.2	6407 \pm 41	3.96 \pm 0.14	-0.61 \pm 0.03	1.63 \pm 0.16	62	9	1.2
HD121370	6227 \pm 75	3.97 \pm 0.03	0.31 \pm 0.03	1.62 \pm 0.01	†	†	0.0	6120 \pm 64	3.91 \pm 0.06	0.3 \pm 0.02	1.62 \pm 0.04	†	†	0.0
HD175955	4608 \pm 48	2.69 \pm 0.14	0.07 \pm 0.04	1.03 \pm 0.03	86	14	0.0	4555 \pm 47	2.66 \pm 0.15	0.1 \pm 0.03	1.04 \pm 0.03	86	14	0.0
HD188512	5133 \pm 62	3.52 \pm 0.16	-0.22 \pm 0.04	0.83 \pm 0.07	34	7	0.0	5074 \pm 64	3.5 \pm 0.17	-0.22 \pm 0.04	0.92 \pm 0.07	34	7	0.0
HD103095	5114 \pm 91	4.37 \pm 0.32	-1.39 \pm 0.08	0.66 \pm 0.12	79	9	2.0	5215 \pm 95	4.66 \pm 0.21	-1.31 \pm 0.05	0.75 \pm 0.18	82	9	2.0
HD224930	5391 \pm 44	4.14 \pm 0.13	-0.9 \pm 0.03	0.79 \pm 0.08	76	11	2.0	5474 \pm 70	4.34 \pm 0.2	-0.82 \pm 0.04	0.7 \pm 0.12	81	11	2.0
GES-K2 Stars (Worley et al. 2020)														
22074607–1055493	4833 \pm 44	2.32 \pm 0.13	-1.03 \pm 0.03	1.22 \pm 0.02	138	16	2.7	4778 \pm 42	2.33 \pm 0.13	-0.99 \pm 0.03	1.23 \pm 0.02	138	16	2.7
22172723–1633039	4597 \pm 28	2.1 \pm 0.1	-0.82 \pm 0.02	1.32 \pm 0.01	136	15	2.5	4540 \pm 26	2.08 \pm 0.09	-0.81 \pm 0.02	1.36 \pm 0.01	136	15	2.5
22094505–1051031	4371 \pm 60	2.04 \pm 0.18	-0.5 \pm 0.05	1.57 \pm 0.03	134	13	0.0	4299 \pm 46	1.95 \pm 0.15	-0.49 \pm 0.05	1.6 \pm 0.04	133	13	0.0
22075605–1535081	4740 \pm 23	3.01 \pm 0.07	-0.01 \pm 0.01	1.17 \pm 0.01	151	17	0.0	4696 \pm 21	3.0 \pm 0.06	0.0 \pm 0.01	1.22 \pm 0.02	148	17	0.0
22072959–1530438	4957 \pm 19	3.32 \pm 0.05	-0.1 \pm 0.01	1.04 \pm 0.02	156	17	0.0	4892 \pm 18	3.27 \pm 0.05	-0.1 \pm 0.01	1.09 \pm 0.02	156	17	0.0
22391293–1502196	4840 \pm 20	3.08 \pm 0.06	-0.07 \pm 0.01	1.21 \pm 0.01	146	16	0.0	4776 \pm 20	3.02 \pm 0.06	-0.06 \pm 0.01	1.25 \pm 0.01	146	16	0.0

Table 3 *continued*

Table 3 (*continued*)

Star Name	LTE						NLTE							
	T_{eff} (K)	$\log g$ (cgs)	[Fe/H] (dex)	v_{mic} (km s $^{-1}$)	$N_{\text{Fe I}}$	$N_{\text{Fe II}}$	$\chi_{\text{Fe I}}$ cutoff (ev)	T_{eff} (K)	$\log g$ (cgs)	[Fe/H] (dex)	v_{mic} (km s $^{-1}$)	$N_{\text{Fe I}}$	$N_{\text{Fe II}}$	$\chi_{\text{Fe I}}$ cutoff (ev)
22390396–1500420	4630±30	2.98±0.09	-0.03±0.02	1.41±0.02	123	15	0.0	4586±28	2.95±0.09	-0.01±0.02	1.42±0.02	123	15	0.0
22035226–1457037	5015±15	3.31±0.04	-0.31±0.01	1.03±0.01	167	15	0.0	4950±15	3.26±0.04	-0.31±0.01	1.07±0.01	167	15	0.0
22071748–1455524	4706±19	2.71±0.06	-0.3±0.01	1.22±0.01	156	17	0.0	4646±19	2.68±0.07	-0.29±0.01	1.27±0.01	151	17	0.0
22033684–1449366	4834±19	2.59±0.06	-0.38±0.01	1.35±0.01	154	17	0.0	4742±17	2.5±0.06	-0.38±0.01	1.39±0.01	153	17	0.0
22072768–1440392	4601±25	2.88±0.08	0.04±0.02	1.22±0.02	131	15	0.0	4558±25	2.86±0.07	0.06±0.02	1.21±0.02	132	15	0.0
22254071–1431281	4893±28	2.6±0.1	-0.34±0.02	1.56±0.01	125	11	0.0	4812±26	2.55±0.1	-0.34±0.02	1.61±0.01	125	11	0.0
22243423–1430033	4531±34	2.65±0.11	0.18±0.03	1.5±0.02	94	15	0.0	4497±33	2.65±0.11	0.21±0.03	1.5±0.02	94	15	0.0
22235672–1428420	4755±17	2.85±0.06	-0.22±0.01	1.22±0.01	148	15	0.0	4697±17	2.82±0.06	-0.21±0.01	1.26±0.01	146	15	0.0
22235003–1422417	4753±31	3.35±0.08	0.3±0.02	1.23±0.03	119	14	0.0	4720±31	3.32±0.07	0.31±0.02	1.25±0.03	119	14	0.0
22175268–1344270	4773±18	2.57±0.07	-0.36±0.01	1.45±0.01	153	17	0.0	4702±17	2.52±0.07	-0.36±0.01	1.49±0.01	153	17	0.0
22250508–1341415	4741±20	2.77±0.07	-0.09±0.01	1.23±0.01	145	16	0.0	4662±19	2.69±0.06	-0.08±0.01	1.25±0.01	145	16	0.0
22174405–1338287	4792±17	2.81±0.06	-0.34±0.01	1.21±0.01	165	13	0.0	4728±17	2.76±0.06	-0.34±0.01	1.27±0.01	158	13	0.0
22185037–1257588	4528±25	2.69±0.08	-0.04±0.02	1.15±0.02	137	15	0.0	4491±25	2.68±0.08	-0.02±0.02	1.16±0.02	136	15	0.0
22204635–1245072	4804±23	3.35±0.06	0.19±0.01	1.02±0.02	143	14	0.0	4761±23	3.32±0.06	0.2±0.02	1.04±0.03	143	14	0.0
22195215–1234594	4707±26	2.72±0.08	-0.08±0.02	1.3±0.01	132	14	0.0	4653±24	2.7±0.08	-0.06±0.01	1.32±0.01	132	14	0.0
21563608–1202424	4792±19	3.13±0.06	-0.28±0.01	1.07±0.02	161	13	0.0	4738±19	3.08±0.06	-0.27±0.01	1.11±0.02	161	13	0.0
21590887–1159078	4678±26	2.71±0.08	-0.0±0.02	1.31±0.01	130	14	0.0	4623±25	2.68±0.08	0.02±0.02	1.32±0.01	130	14	0.0
2201504–1153022	4743±19	2.82±0.06	-0.25±0.01	1.29±0.01	155	16	0.0	4699±19	2.83±0.06	-0.23±0.01	1.33±0.01	150	16	0.0
22013369–1141245	4636±18	2.47±0.06	-0.43±0.01	1.31±0.01	152	16	0.0	4575±16	2.43±0.06	-0.41±0.01	1.34±0.01	153	16	0.0
22021848–1139147	4638±30	2.89±0.09	0.17±0.02	1.34±0.02	119	16	0.0	4597±28	2.87±0.09	0.19±0.02	1.35±0.02	119	16	0.0
22104061–1125284	4603±27	2.79±0.08	0.04±0.02	1.29±0.02	123	15	0.0	4559±26	2.77±0.08	0.06±0.02	1.29±0.02	123	15	0.0
220744730–1059405	4757±23	3.0±0.06	0.0±0.01	1.16±0.02	149	17	0.0	4712±21	3.0±0.06	0.01±0.01	1.22±0.02	146	17	0.0
22114557–0957433	4885±18	3.34±0.05	-0.16±0.01	1.03±0.02	153	16	0.0	4830±17	3.29±0.05	-0.16±0.01	1.06±0.02	153	16	0.0
22105372–0956597	4705±17	2.86±0.06	-0.37±0.01	1.09±0.01	158	16	0.0	4642±16	2.8±0.06	-0.37±0.01	1.17±0.01	148	16	0.0
22083624–0948555	4816±33	3.01±0.1	0.42±0.02	1.34±0.02	106	12	0.0	4769±33	3.0±0.09	0.45±0.02	1.34±0.02	106	12	0.0
22091180–0944335	4849±17	3.4±0.05	-0.24±0.01	0.9±0.02	159	13	0.0	4803±16	3.37±0.05	-0.23±0.01	0.93±0.02	159	13	0.0
22102197–0923157	4931±17	2.67±0.06	-0.2±0.01	1.32±0.01	143	15	0.0	4846±17	2.61±0.06	-0.2±0.01	1.37±0.01	142	15	0.0
22013945–0909229	4664±29	3.19±0.07	0.33±0.03	1.16±0.03	107	14	0.0	4634±29	3.17±0.07	0.34±0.03	1.17±0.03	107	14	0.0
22052550–0854435	4845±17	2.56±0.06	-0.32±0.01	1.49±0.01	156	13	0.0	4766±17	2.51±0.06	-0.32±0.01	1.53±0.01	155	13	0.0
22052114–0848002	4750±18	2.64±0.06	-0.36±0.01	1.22±0.01	158	15	0.0	4705±18	2.67±0.07	-0.35±0.01	1.31±0.01	145	15	0.0
22055148–0840028	4700±20	2.91±0.06	-0.27±0.01	1.19±0.01	162	12	0.0	4646±19	2.88±0.06	-0.27±0.01	1.24±0.01	158	12	0.0
22062074–0809079	4694±25	2.91±0.07	-0.01±0.02	1.23±0.02	136	14	0.0	4645±25	2.89±0.07	0.01±0.02	1.24±0.02	136	14	0.0

Table 3 *continued*

Table 3 (*continued*)

Star Name	LTE						NLTE							
	T_{eff} (K)	$\log g$ (cgs)	[Fe/H] (dex)	v_{mic} (km s $^{-1}$)	$N_{\text{Fe I}}$	$N_{\text{Fe I}}$	$\chi_{\text{Fe I}}$ cutoff (ev)	T_{eff} (K)	$\log g$ (cgs)	[Fe/H] (dex)	v_{mic} (km s $^{-1}$)	$N_{\text{Fe I}}$	$N_{\text{Fe II}}$	$\chi_{\text{Fe I}}$ cutoff (ev)
22291753–0806290	4664±19	2.9±0.06	-0.3±0.01	1.19±0.01	161	15	0.0	4615±17	2.87±0.06	-0.29±0.01	1.23±0.01	158	15	0.0
22122727–0719010	4428±27	2.46±0.1	-0.15±0.03	1.36±0.01	139	15	0.0	4389±27	2.46±0.09	-0.13±0.02	1.36±0.02	139	15	0.0
22292970–0713347	4833±19	2.64±0.06	-0.22±0.01	1.42±0.01	153	17	0.0	4757±17	2.59±0.06	-0.21±0.01	1.46±0.01	153	17	0.0
22130580–0658576	4594±27	2.78±0.09	-0.03±0.02	1.37±0.01	132	14	0.0	4550±26	2.76±0.08	-0.01±0.02	1.38±0.02	132	14	0.0
22092886–0617515	4731±21	3.02±0.06	-0.26±0.01	1.13±0.02	160	16	0.0	4693±22	3.02±0.06	-0.24±0.01	1.17±0.02	154	16	0.0
22153043–0617291	4942±16	2.5±0.06	-0.51±0.01	1.4±0.01	163	17	0.0	4850±17	2.44±0.06	-0.52±0.01	1.49±0.01	149	17	0.0
22092416–0610474	4789±24	2.7±0.08	-0.0±0.02	1.36±0.01	138	16	0.0	4726±24	2.67±0.08	0.03±0.01	1.38±0.01	139	16	0.0
22085850–0608204	4839±20	2.64±0.07	-0.32±0.01	1.36±0.01	148	9	0.0	4758±20	2.59±0.07	-0.32±0.01	1.4±0.01	147	10	0.0
22375413–0604257	4770±27	2.84±0.08	0.12±0.02	1.32±0.01	128	16	0.0	4712±26	2.81±0.08	0.13±0.02	1.36±0.01	129	16	0.0
22354169–0543252	4735±22	3.0±0.06	0.1±0.01	1.1±0.02	136	15	0.0	4693±21	3.0±0.06	0.13±0.01	1.11±0.02	139	15	0.0
22362945–0540124	4825±20	3.16±0.06	-0.17±0.01	1.17±0.02	150	15	0.0	4769±19	3.12±0.06	-0.17±0.01	1.21±0.02	150	15	0.0
22342769–0522505	4645±22	2.94±0.07	-0.1±0.01	1.19±0.02	153	15	0.0	4602±22	2.93±0.07	-0.09±0.01	1.21±0.02	151	15	0.0
22342069–0520353	4763±20	3.28±0.05	0.04±0.01	0.97±0.02	154	16	0.0	4720±19	3.24±0.05	0.05±0.01	0.99±0.02	154	16	0.0
22344800–0516214	4842±23	3.25±0.06	0.11±0.01	1.17±0.02	136	17	0.0	4790±21	3.21±0.06	0.12±0.01	1.19±0.02	136	17	0.0
<i>R</i> -Process Alliance Stars (Hansen et al. 2018)														
J03193531–3250433	6353±24	3.0±0.05	-2.97±0.01	2.81±0.15	11	5	2.7	6345±201	3.75±0.05	-2.77±0.1	2.8±0.15	11	5	2.7
J02401075–1416290	6041±116	4.4±0.19	-0.89±0.08	0.87±0.12	35	9	1.2	5991±107	4.34±0.18	-0.85±0.08	0.74±0.13	35	9	1.2
J0023067–1631428	5354±175	2.93±0.47	-2.53±0.12	2.12±0.2	28	13	2.7	5297±24	3.0±0.05	-2.45±0.03	1.7±0.17	28	13	2.7
J01134657–2727374	5216±151	2.46±0.42	-1.77±0.12	2.23±0.07	26	6	2.7	5221±147	2.65±0.35	-1.66±0.11	2.18±0.09	26	6	2.7
J00133067–125594	4620±30	0.07±0.05	-2.78±0.03	1.82±0.07	36	9	2.7	4517±21	0.11±0.09	-2.73±0.03	1.8±0.06	36	9	2.7
J19215077–4452545	4659±23	0.1±0.07	-2.55±0.03	1.77±0.05	41	7	2.7	4561±32	0.13±0.11	-2.46±0.05	1.76±0.06	41	6	2.7
J23265258–0159248	4645±53	0.22±0.13	-3.13±0.04	1.94±0.08	32	15	2.7	4598±27	0.31±0.1	-3.0±0.03	1.88±0.09	32	15	2.7
J00403260–5122491	5547±59	4.01±0.22	-2.22±0.03	1.29±0.15	37	10	2.7	5495±75	3.93±0.23	-2.2±0.04	1.17±0.14	37	10	2.7
J15271353–2336177	6001±24	4.0±0.05	-2.16±0.01	1.64±0.08	48	13	2.7	6001±24	4.0±0.05	-2.11±0.02	1.82±0.13	48	13	2.7
J01530024–3417360	5171±65	2.96±0.13	-1.73±0.05	1.45±0.05	62	14	2.7	5116±93	2.96±0.18	-1.71±0.08	1.4±0.05	62	14	2.7
J16024498–1521016	5145±128	2.95±0.26	-1.99±0.1	1.69±0.05	44	13	2.7	5085±157	2.93±0.35	-1.99±0.14	1.69±0.05	44	13	2.7
J20514971–6158008	5221±145	2.97±0.29	-1.94±0.11	1.53±0.07	47	14	2.7	5187±134	3.01±0.29	-1.9±0.11	1.48±0.07	47	14	2.7
J16103106+1003055	5354±200	2.33±0.51	-2.44±0.13	1.68±0.21	32	3	1.2	5411±118	2.83±0.29	-2.26±0.13	1.5±0.09	32	3	1.2
J16184302–0630558	5293±103	1.14±0.29	-2.84±0.05	2.1±0.09	38	11	1.2	5339±114	2.1±0.39	-2.54±0.08	2.39±0.35	36	11	1.2
J21063474–4957500	5365±23	3.0±0.05	-2.89±0.02	1.53±0.12	33	9	2.7	5254±24	2.99±0.05	-2.88±0.02	1.26±0.09	33	9	2.7
J00021668–2453494	5140±160	1.81±0.48	-1.85±0.11	1.87±0.15	39	11	2.7	5185±145	2.24±0.39	-1.71±0.09	2.03±0.15	40	11	2.7
J02355867–6745520	4661±108	0.81±0.25	-1.7±0.08	2.09±0.12	30	10	2.7	4565±96	0.77±0.21	-1.66±0.07	2.14±0.08	31	10	2.7

Table 3 *continued*

Table 3 (*continued*)

Star Name	LTE						NLTE							
	T_{eff} (K)	$\log g$ (cgs)	[Fe/H] (dex)	v_{mic} (km s $^{-1}$)	$N_{\text{Fe I}}$	$N_{\text{Fe II}}$	$\chi_{\text{Fe I}}$ cutoff (ev)	T_{eff} (K)	$\log g$ (cgs)	[Fe/H] (dex)	v_{mic} (km s $^{-1}$)	$N_{\text{Fe I}}$	$N_{\text{Fe II}}$	$\chi_{\text{Fe I}}$ cutoff (ev)
J13164824–2743251	4821±95	1.78±0.3	-1.86±0.08	1.43±0.06	65	14	2.7	4806±91	1.96±0.27	-1.79±0.08	1.48±0.06	66	14	2.7
J14232679–2834200	4882±200	1.57±0.53	-2.19±0.17	1.39±0.08	45	9	2.7	4902±180	1.87±0.49	-2.08±0.15	1.43±0.07	46	9	2.7
J14301385–2317388	4353±51	0.67±0.13	-1.68±0.04	2.37±0.04	54	13	2.7	4298±39	0.65±0.11	-1.64±0.03	2.43±0.03	54	13	2.7
J15575183–0839549	4585±71	1.29±0.29	-1.82±0.07	1.92±0.06	55	16	2.7	4564±72	1.42±0.28	-1.74±0.07	1.96±0.04	56	16	2.7
J16080681–3215592	4531±27	0.49±0.18	-2.28±0.03	1.73±0.02	89	15	1.2	4460±26	0.63±0.14	-2.25±0.03	1.81±0.02	89	15	1.2
J17273886–5132928	5068±143	1.28±0.41	-1.85±0.08	2.07±0.16	52	13	2.7	5159±113	1.87±0.32	-1.67±0.06	2.28±0.13	52	13	2.7
J17334285–5121550	4864±153	0.99±0.37	-2.02±0.1	1.93±0.11	46	14	2.7	4891±167	1.22±0.44	-1.88±0.12	2.04±0.1	47	14	2.7
J18024226–4404426	4654±89	1.6±0.3	-1.65±0.08	1.94±0.04	47	8	2.7	4625±88	1.7±0.29	-1.57±0.08	1.97±0.05	48	8	2.7
J19014952–4844359	4602±26	1.06±0.11	-2.17±0.03	1.65±0.01	72	7	0.0	4549±27	1.14±0.11	-2.12±0.03	1.73±0.01	73	7	0.0
J19324858–5908019	4427±102	1.66±0.3	-2.13±0.08	1.72±0.08	29	7	2.7	4411±96	1.77±0.29	-2.09±0.08	1.75±0.09	29	7	2.7
J20144608–5635300	4828±115	1.36±0.39	-1.98±0.09	1.61±0.16	15	11	2.7	4773±130	1.53±0.41	-1.95±0.1	1.84±0.15	16	11	2.7
J22444701–5617540	4395±107	0.79±0.23	-2.09±0.08	1.8±0.09	22	6	2.7	4326±102	0.79±0.23	-2.09±0.08	1.95±0.08	22	6	2.7
J22492756–2238289	4768±105	1.09±0.31	-2.0±0.08	1.93±0.12	44	7	2.7	4782±102	1.38±0.29	-1.89±0.09	2.11±0.1	44	7	2.7
J22531984–2248555	4577±87	1.09±0.29	-2.11±0.07	1.58±0.07	52	14	2.7	4578±82	1.31±0.27	-2.03±0.07	1.66±0.07	53	14	2.7
J23362202–5607498	4459±106	0.81±0.24	-2.29±0.07	2.16±0.17	13	8	2.7	4495±109	0.9±0.27	-2.23±0.08	2.4±0.18	14	8	2.7
J00002259–1302275	4835±117	1.72±0.47	-2.46±0.1	2.4±0.33	44	5	0.0	4739±99	2.03±0.57	-2.52±0.09	2.52±0.3	43	5	0.0
J00021222–2241388	5180±137	2.03±0.43	-2.16±0.07	1.74±0.21	46	8	2.7	5164±113	2.34±0.37	-2.05±0.05	1.78±0.27	46	8	2.7
J00400685–4325183	4458±156	0.66±0.45	-2.65±0.13	2.06±0.14	25	7	2.7	4422±133	0.65±0.43	-2.55±0.13	2.04±0.14	25	8	2.7
J00453330–7457294	4727±37	1.49±0.17	-2.25±0.04	1.77±0.02	83	15	1.2	4684±35	1.65±0.16	-2.2±0.04	1.76±0.02	83	15	1.2
J01202234–5425582	5133±131	2.33±0.44	-2.11±0.08	1.45±0.16	48	9	2.7	5123±118	2.59±0.41	-2.01±0.08	1.39±0.19	48	9	2.7
J01293113–1600454	4678±133	1.09±0.41	-3.07±0.09	2.1±0.16	26	11	2.7	4800±134	1.76±0.35	-2.84±0.11	2.18±0.15	26	11	2.7
J01425422–5032488	5140±73	2.52±0.23	-2.18±0.06	1.66±0.06	49	15	2.7	5132±84	2.74±0.27	-2.08±0.06	1.6±0.11	49	15	2.7
J01430726–6445174	4582±66	0.51±0.25	-3.11±0.05	1.86±0.1	28	9	2.7	4563±76	0.9±0.27	-2.95±0.07	1.79±0.07	29	9	2.7
J01451951–2800583	4445±59	0.46±0.25	-2.89±0.05	1.63±0.03	31	12	2.7	4396±61	0.51±0.23	-2.8±0.06	1.61±0.03	31	12	2.7
J01490794–4911429	4691±72	0.77±0.24	-3.05±0.05	1.84±0.07	29	14	2.7	4845±81	1.61±0.22	-2.79±0.07	1.98±0.08	29	14	2.7
J02040793–312556	4556±43	0.56±0.2	-3.17±0.04	2.1±0.06	67	16	1.2	4603±55	1.15±0.19	-3.01±0.07	2.24±0.07	66	16	1.2
J02165716–7547064	4531±64	0.48±0.26	-2.6±0.06	2.16±0.04	40	6	2.7	4537±65	0.7±0.24	-2.44±0.06	2.15±0.03	40	11	2.7
J02412152–1823576	4270±25	0.43±0.14	-2.3±0.02	1.52±0.03	64	9	1.2	4239±24	0.45±0.12	-2.31±0.02	1.71±0.02	63	10	1.2
J02441479–5158241	5223±120	2.28±0.4	-2.78±0.08	2.0±0.1	36	14	2.7	5201±79	2.7±0.26	-2.64±0.06	1.94±0.12	36	14	2.7
J02462013–1518419	5047±265	1.9±0.73	-2.77±0.2	2.69±0.22	15	9	2.7	5043±180	2.31±0.47	-2.61±0.13	2.62±0.24	15	9	2.7
J02500719–5145148	4575±37	0.96±0.18	-2.34±0.04	1.96±0.03	85	12	1.2	4527±38	1.11±0.16	-2.29±0.04	2.01±0.03	85	12	1.2
J03563703–5838281	4614±99	0.69±0.34	-2.78±0.08	2.1±0.06	30	9	2.7	4713±110	1.36±0.33	-2.55±0.1	2.07±0.06	30	9	2.7

Table 3 *continued*

NLTE STELLAR PARAMETERS WITH LOTUS

Table 3 (*continued*)

Star Name	LTE						NLTE						
	T_{eff} (K)	$\log g$ (cgs)	[Fe/H] (dex)	v_{mic} (km s $^{-1}$)	$N_{\text{Fe I}}$	$N_{\text{Fe I}}$ cutoff (ev)	T_{eff} (K)	$\log g$ (cgs)	[Fe/H] (dex)	v_{mic} (km s $^{-1}$)	$N_{\text{Fe I}}$	$N_{\text{Fe II}}$	$\chi_{\text{Fe I,cutoff}}$ (eV)
J04121388–1205050	4601±57	0.48±0.25	-2.82±0.06	2.21±0.05	22	7	4515±48	0.57±0.18	-2.78±0.06	2.33±0.05	22	7	1.2
J14033542–3335257	5040±127	1.97±0.32	-2.69±0.09	1.76±0.11	53	10	5116±102	2.48±0.28	-2.49±0.08	1.7±0.15	53	10	2.7
J14164084–2422000	4555±95	0.53±0.33	-2.78±0.07	1.77±0.06	38	16	4475±115	0.64±0.36	-2.7±0.1	1.77±0.05	38	16	2.7
J14325334–4125494	4729±127	1.51±0.36	-3.14±0.1	1.55±0.12	34	10	4791±113	1.95±0.31	-2.99±0.1	1.62±0.11	34	10	2.7
J14381119–2120085	4458±50	0.53±0.27	-2.44±0.04	1.9±0.03	47	14	4368±57	0.61±0.25	-2.41±0.05	1.91±0.03	48	13	2.7
J15260106–0911388	4697±119	0.72±0.38	-2.79±0.08	2.16±0.13	29	11	4784±128	1.37±0.36	-2.55±0.11	2.13±0.13	29	11	2.7
J15582962–1224344	5298±175	1.37±0.38	-2.58±0.09	2.63±0.22	44	16	5222±119	2.09±0.29	-2.39±0.09	2.73±0.21	44	16	2.7
J16095117–0941174	4620±58	0.57±0.24	-2.82±0.04	1.86±0.05	39	15	4767±70	1.39±0.18	-2.55±0.06	1.91±0.05	39	15	2.7
J170931199–6027271	4525±55	0.37±0.24	-2.49±0.06	2.12±0.05	53	8	4448±50	0.4±0.2	-2.41±0.06	2.11±0.03	53	8	1.2
J17094926–6239285	4611±123	0.88±0.43	-2.49±0.1	1.42±0.09	33	10	4712±118	1.47±0.33	-2.26±0.1	1.35±0.08	33	10	2.7
J17124284–5211479	4745±174	0.99±0.5	-2.77±0.13	1.24±0.12	26	10	4855±158	1.61±0.39	-2.54±0.13	1.28±0.1	26	10	2.7
J17225742–7123000	5019±113	2.36±0.33	-2.55±0.1	1.8±0.09	41	10	4998±97	2.58±0.28	-2.47±0.1	1.7±0.1	41	10	1.2
J17255680–6603395	4666±66	0.49±0.27	-2.66±0.05	2.13±0.05	35	12	4671±77	0.99±0.23	-2.5±0.07	2.05±0.05	35	12	2.7
J17285330–7427532	4760±136	1.1±0.57	-2.18±0.09	1.41±0.13	38	8	4773±95	1.44±0.42	-2.07±0.06	1.45±0.13	38	8	2.7
J17400682–6102129	4594±91	0.93±0.33	-2.52±0.07	1.8±0.05	43	12	4625±96	1.32±0.29	-2.37±0.08	1.8±0.04	43	12	2.7
J17435113–5359333	5198±147	1.85±0.43	-2.28±0.07	2.13±0.24	58	14	5203±121	2.37±0.35	-2.12±0.07	2.13±0.23	58	12	2.7
J18121045–4934495	4526±79	0.6±0.29	-3.03±0.06	2.19±0.09	27	9	4657±89	1.31±0.27	-2.78±0.08	2.2±0.08	27	9	2.7
J18285086–3434203	4706±33	1.16±0.3	-2.4±0.07	1.62±0.07	60	14	4735±88	1.51±0.25	-2.25±0.08	1.64±0.07	60	14	2.7
J18294122–4504000	4572±92	0.71±0.34	-2.67±0.08	1.8±0.05	38	7	4624±96	1.2±0.29	-2.48±0.1	1.73±0.05	38	7	2.7
J18362318–6428124	4700±90	1.17±0.28	-2.77±0.07	1.78±0.07	34	13	4823±91	1.77±0.25	-2.54±0.07	1.79±0.06	34	13	2.7
J18363613–7136597	4574±150	0.56±0.43	-2.65±0.12	2.1±0.1	41	9	4556±91	0.58±0.32	-2.46±0.09	2.02±0.05	41	13	2.7
J18562774–7251331	4641±65	0.48±0.32	-2.32±0.06	1.74±0.05	38	4	4538±88	0.56±0.33	-2.26±0.09	1.75±0.03	38	4	2.7
J19161821–5544454	4449±21	0.23±0.17	-2.4±0.02	1.99±0.09	32	10	4377±22	0.3±0.18	-2.38±0.03	2.12±0.08	32	10	2.7
J19172402–4211240	4568±88	0.59±0.32	-2.83±0.07	1.96±0.08	53	13	4681±109	1.25±0.3	-2.59±0.1	1.99±0.08	53	13	2.7
J19173310–6628545	4608±160	0.89±0.52	-2.81±0.12	2.53±0.13	19	9	4668±164	1.35±0.47	-2.63±0.14	2.49±0.1	19	9	2.7
J19202070–6627202	4426±31	0.59±0.21	-2.4±0.03	1.45±0.03	81	11	4451±38	1.04±0.16	-2.34±0.04	1.6±0.04	78	11	1.2
J19232518–5833410	5029±209	1.87±0.69	-2.17±0.13	2.05±0.36	36	7	5039±155	2.21±0.57	-2.06±0.09	2.14±0.35	36	7	2.7
J19345497–5751400	4841±204	2.09±0.66	-2.33±0.17	2.41±0.14	11	5	4841±190	2.44±0.67	-2.23±0.15	2.29±0.12	11	5	2.7
J19494025–5424113	4648±129	0.87±0.41	-2.83±0.1	2.09±0.1	25	9	4733±123	1.47±0.34	-2.62±0.11	2.08±0.06	25	9	2.7
J19534978–5940001	4708±45	0.49±0.19	-2.83±0.04	2.46±0.05	41	10	4672±62	0.96±0.21	-2.65±0.08	2.24±0.05	43	10	1.2
J19594558–2549075	4523±72	0.46±0.29	-2.5±0.05	2.15±0.05	42	15	4442±81	0.52±0.26	-2.45±0.07	2.16±0.05	42	15	2.7
J20093393–3410273	4410±39	1.64±0.15	-2.19±0.02	2.18±0.08	62	7	4312±20	1.77±0.18	-2.22±0.02	2.19±0.07	62	7	1.2

Table 3 *continued*

Table 3 (*continued*)

Star Name	LTE						NLTE						
	T_{eff} (K)	$\log g$ (cgs)	[Fe/H] (dex)	v_{mic} (km s $^{-1}$)	N_{FeI}	$\chi_{\text{FeI cutoff}}$ (ev)	T_{eff} (K)	$\log g$ (cgs)	[Fe/H] (dex)	v_{mic} (km s $^{-1}$)	N_{FeI}	N_{FeII}	$\chi_{\text{FeI cutoff}}$ (ev)
J20165357-0503592	4546±105	0.6±0.33	-2.96±0.09	2.11±0.11	35	7	4639±127	1.21±0.36	-2.74±0.13	2.13±0.09	35	7	2.7
J20303339-2519500	4378±17	0.06±0.05	-2.29±0.02	1.75±0.03	65	16	4312±23	0.12±0.11	-2.24±0.02	1.83±0.05	65	16	2.7
J20313531-3127319	4658±107	0.7±0.34	-2.72±0.08	1.96±0.09	28	10	4759±125	1.36±0.33	-2.49±0.11	1.98±0.11	28	10	2.7
J20445584-2250597	4330±44	0.5±0.23	-2.49±0.03	2.03±0.03	54	14	4266±51	0.5±0.24	-2.49±0.04	2.21±0.04	55	14	2.7
J20492765-5124440	4503±67	0.55±0.28	-2.49±0.06	1.81±0.04	38	9	4492±76	0.87±0.27	-2.39±0.07	1.83±0.03	38	9	2.7
J20542346-0033097	4414±57	0.52±0.27	-2.87±0.05	2.53±0.06	36	13	4402±78	0.76±0.27	-2.77±0.08	2.49±0.05	37	13	2.7
J20560913-1331176	4615±53	0.98±0.2	-2.5±0.04	1.65±0.02	58	17	4668±54	1.41±0.16	-2.34±0.05	1.63±0.02	58	17	2.7
J21023752-5316132	5198±289	2.4±0.94	-2.32±0.22	1.36±0.36	29	9	5178±162	2.6±0.5	-2.22±0.08	1.22±0.33	29	9	2.7
J21064294-6828266	4830±255	1.7±0.76	-3.1±0.21	2.76±0.17	11	9	4843±251	2.08±0.74	-2.97±0.21	2.79±0.15	11	9	2.7
J21091825-1310062	4746±106	0.97±0.35	-2.51±0.08	1.79±0.06	46	18	4820±103	1.53±0.29	-2.31±0.09	1.8±0.05	46	18	2.7
J21095804-0945400	4493±77	0.68±0.3	-2.85±0.06	1.79±0.07	19	7	4555±83	1.15±0.27	-2.66±0.08	1.77±0.05	19	7	2.7
J21141350-5726363	4515±67	0.51±0.24	-2.95±0.06	1.94±0.05	57	7	4590±79	1.12±0.23	-2.74±0.09	1.96±0.05	57	7	2.7
J21152551-1503309	4505±72	0.52±0.33	-2.32±0.05	1.77±0.06	38	14	4458±82	0.69±0.3	-2.29±0.07	1.86±0.03	37	10	2.7
J21162185-0213420	4418±25	0.08±0.06	-2.33±0.03	1.48±0.04	41	7	4234±43	0.45±0.25	-2.44±0.05	1.86±0.05	37	2	2.7
J21224590-4641030	4743±123	1.11±0.41	-2.9±0.09	2.23±0.13	24	11	4842±125	1.75±0.33	-2.68±0.11	2.25±0.12	24	11	2.7
J21262525-2144243	4362±61	0.57±0.26	-2.93±0.06	1.84±0.04	52	10	4400±66	0.96±0.23	-2.78±0.07	1.82±0.04	52	10	2.7
J21291592-4236219	4602±104	0.82±0.38	-2.63±0.08	2.08±0.07	43	14	4673±110	1.34±0.32	-2.44±0.1	2.05±0.06	43	14	2.7
J21370807-0927347	4507±119	0.72±0.5	-2.53±0.1	1.86±0.09	34	8	4364±109	0.63±0.37	-2.52±0.11	1.84±0.08	36	8	2.7
J21513595-0543398	4489±71	0.44±0.24	-2.59±0.06	2.02±0.04	42	14	4412±52	0.49±0.2	-2.55±0.05	2.08±0.05	42	14	2.7
J22021636-0536483	4695±58	0.74±0.25	-2.76±0.05	2.03±0.07	42	10	4731±68	1.31±0.24	-2.57±0.08	2.06±0.05	42	10	2.7
J22163596+0246171	4759±114	1.41±0.34	-2.51±0.1	1.49±0.06	49	7	4761±104	1.7±0.28	-2.39±0.1	1.44±0.05	49	7	2.7
J22595884-1554182	4552±101	0.57±0.33	-2.73±0.08	2.14±0.05	44	12	4543±118	0.87±0.37	-2.57±0.11	2.05±0.05	44	12	2.7
J23022289-6833233	5232±162	2.23±0.51	-2.52±0.11	1.79±0.17	39	7	5227±144	2.72±0.49	-2.39±0.1	1.82±0.29	39	7	2.7
J23044914-4243477	4670±98	1.58±0.32	-2.48±0.09	0.79±0.07	26	12	4634±91	1.68±0.27	-2.43±0.09	0.77±0.07	26	12	2.7
J23130003-4507066	4589±83	0.57±0.32	-2.68±0.06	1.79±0.06	35	13	4675±100	1.17±0.31	-2.46±0.09	1.79±0.07	35	13	2.7
J23310716-0223301	4873±228	1.08±0.64	-2.5±0.16	2.06±0.18	12	3	4938±201	1.68±0.56	-2.28±0.16	2.06±0.2	12	3	2.7

Note—

† For HD121370, parameters are obtained with the average of runs inputting 3 different EW line lists: EPINARBO in Heiter et al. (2015), BOLOGNA in Heiter et al. (2015) and Takeda et al. (2005). In LTE, there are $N_{\text{FeI}}=79$, 121, 46, $N_{\text{FeI}}=6$, 9, 4 lines in these three line list respectively; In NLTE, $N_{\text{FeI}}=79$, 121, 47, $N_{\text{FeI}}=6$, 9, 4 lines in machine-readable form.)

REFERENCES

- Ahumada, R., Prieto, C. A., Almeida, A., et al. 2020, ApJS, 249, 3, doi: [10.3847/1538-4365/ab929e](https://doi.org/10.3847/1538-4365/ab929e)
- Amarsi, A. M., Liljegren, S., & Nissen, P. E. 2022, A&A, 668, A68, doi: [10.1051/0004-6361/202244542](https://doi.org/10.1051/0004-6361/202244542)
- Amarsi, A. M., Lind, K., Asplund, M., Barklem, P. S., & Collet, R. 2016, MNRAS, 463, 1518, doi: [10.1093/mnras/stw2077](https://doi.org/10.1093/mnras/stw2077)
- Amarsi, A. M., Lind, K., Osorio, Y., et al. 2020, A&A, 642, A62, doi: [10.1051/0004-6361/202038650](https://doi.org/10.1051/0004-6361/202038650)
- Asplund, M. 2005, ARA&A, 43, 481, doi: [10.1146/annurev.astro.42.053102.134001](https://doi.org/10.1146/annurev.astro.42.053102.134001)
- Asplund, M., Grevesse, N., Sauval, A. J., & Scott, P. 2009, ARA&A, 47, 481, doi: [10.1146/annurev.astro.46.060407.145222](https://doi.org/10.1146/annurev.astro.46.060407.145222)
- Astropy Collaboration, Robitaille, T. P., Tollerud, E. J., et al. 2013, A&A, 558, A33, doi: [10.1051/0004-6361/201322068](https://doi.org/10.1051/0004-6361/201322068)
- Astropy Collaboration, Price-Whelan, A. M., Sipőcz, B. M., et al. 2018, AJ, 156, 123, doi: [10.3847/1538-3881/aabc4f](https://doi.org/10.3847/1538-3881/aabc4f)
- Audouze, J., & Tinsley, B. M. 1976, ARA&A, 14, 43, doi: [10.1146/annurev.aa.14.090176.000355](https://doi.org/10.1146/annurev.aa.14.090176.000355)
- Barklem, P. S. 2018, A&A, 612, A90, doi: [10.1051/0004-6361/201732365](https://doi.org/10.1051/0004-6361/201732365)
- Bergemann, M., Lind, K., Collet, R., Magic, Z., & Asplund, M. 2012, MNRAS, 427, 27, doi: [10.1111/j.1365-2966.2012.21687.x](https://doi.org/10.1111/j.1365-2966.2012.21687.x)
- Bernstein, R., Shectman, S. A., Gunnels, S. M., Mochnacki, S., & Athey, A. E. 2003, in Instrument Design and Performance for Optical/Infrared Ground-based Telescopes, ed. M. Iye & A. F. M. Moorwood, Vol. 4841, International Society for Optics and Photonics (SPIE), 1694 – 1704, doi: [10.1117/12.461502](https://doi.org/10.1117/12.461502)
- Blanco-Cuaresma, S. 2019, MNRAS, 486, 2075, doi: [10.1093/mnras/stz549](https://doi.org/10.1093/mnras/stz549)
- Blanco-Cuaresma, S., Soubiran, C., Heiter, U., & Jofré, P. 2014, A&A, 569, A111, doi: [10.1051/0004-6361/201423945](https://doi.org/10.1051/0004-6361/201423945)
- Boeche, C., & Grebel, E. K. 2016, A&A, 587, A2, doi: [10.1051/0004-6361/201526758](https://doi.org/10.1051/0004-6361/201526758)
- Brodtkorb, P. A., & D'Errico, J. 2015, numdifftools 0.9.11, <https://github.com/pbrod/numdifftools>
- Buitinck, L., Louppe, G., Blondel, M., et al. 2013, in ECML PKDD Workshop: Languages for Data Mining and Machine Learning, 108–122
- Cantat-Gaudin, T., Donati, P., Pancino, E., et al. 2014, A&A, 562, A10, doi: [10.1051/0004-6361/201322533](https://doi.org/10.1051/0004-6361/201322533)
- Casagrande, L., Ramírez, I., Meléndez, J., Bessell, M., & Asplund, M. 2010, A&A, 512, A54, doi: [10.1051/0004-6361/200913204](https://doi.org/10.1051/0004-6361/200913204)
- Casagrande, L., Schönrich, R., Asplund, M., et al. 2011, A&A, 530, A138, doi: [10.1051/0004-6361/201016276](https://doi.org/10.1051/0004-6361/201016276)
- Collette, A. 2013, Python and HDF5 (O'Reilly)
- Creevey, O., Grundahl, F., Thévenin, F., et al. 2019, A&A, 625, A33, doi: [10.1051/0004-6361/201834721](https://doi.org/10.1051/0004-6361/201834721)
- Creevey, O. L., Thévenin, F., Boyajian, T. S., et al. 2012, A&A, 545, A17, doi: [10.1051/0004-6361/201219651](https://doi.org/10.1051/0004-6361/201219651)
- Creevey, O. L., Thévenin, F., Berio, P., et al. 2015, A&A, 575, A26, doi: [10.1051/0004-6361/201424310](https://doi.org/10.1051/0004-6361/201424310)
- Cui, X.-Q., Zhao, Y.-H., Chu, Y.-Q., et al. 2012, Research in Astronomy and Astrophysics, 12, 1197, doi: [10.1088/1674-4527/12/9/003](https://doi.org/10.1088/1674-4527/12/9/003)
- Dalton, G., Trager, S., Abrams, D. C., et al. 2016, in Society of Photo-Optical Instrumentation Engineers (SPIE) Conference Series, Vol. 9908, Ground-based and Airborne Instrumentation for Astronomy VI, ed. C. J. Evans, L. Simard, & H. Takami, 99081G, doi: [10.1117/12.2231078](https://doi.org/10.1117/12.2231078)
- de Jong, R. S., Agertz, O., Berbel, A. A., et al. 2019, The Messenger, 175, 3, doi: [10.18727/0722-6691/5117](https://doi.org/10.18727/0722-6691/5117)
- De Silva, G. M., Freeman, K. C., Bland-Hawthorn, J., et al. 2015, MNRAS, 449, 2604, doi: [10.1093/mnras/stv327](https://doi.org/10.1093/mnras/stv327)
- Deng, L.-C., Newberg, H. J., Liu, C., et al. 2012, Research in Astronomy and Astrophysics, 12, 735, doi: [10.1088/1674-4527/12/7/003](https://doi.org/10.1088/1674-4527/12/7/003)
- Dotter, A., Chaboyer, B., Jevremović, D., et al. 2008, ApJS, 178, 89, doi: [10.1086/589654](https://doi.org/10.1086/589654)
- Ezzeddine, R., Frebel, A., & Plez, B. 2017, ApJ, 847, 142, doi: [10.3847/1538-4357/aa8875](https://doi.org/10.3847/1538-4357/aa8875)
- Ezzeddine, R., Merle, T., & Plez, B. 2016, Astronomische Nachrichten, 337, 850, doi: [10.1002/asna.201612384](https://doi.org/10.1002/asna.201612384)

- Ezzeddine, R., Rasmussen, K., Frebel, A., et al. 2020, *ApJ*, 898, 150, doi: [10.3847/1538-4357/ab9d1a](https://doi.org/10.3847/1538-4357/ab9d1a)
- Foreman-Mackey, D. 2016, *The Journal of Open Source Software*, 1, 24, doi: [10.21105/joss.00024](https://doi.org/10.21105/joss.00024)
- Frebel, A., Casey, A. R., Jacobson, H. R., & Yu, Q. 2013, *ApJ*, 769, 57, doi: [10.1088/0004-637X/769/1/57](https://doi.org/10.1088/0004-637X/769/1/57)
- García Pérez, A. E., Allende Prieto, C., Holtzman, J. A., et al. 2016, *AJ*, 151, 144, doi: [10.3847/0004-6256/151/6/144](https://doi.org/10.3847/0004-6256/151/6/144)
- Geman, S., & Geman, D. 1984, *IEEE Transactions on Pattern Analysis and Machine Intelligence*, PAMI-6, 721, doi: [10.1109/TPAMI.1984.4767596](https://doi.org/10.1109/TPAMI.1984.4767596)
- Gerber, J. M., Magg, E., Plez, B., et al. 2022, arXiv e-prints, arXiv:2206.00967. <https://arxiv.org/abs/2206.00967>
- Giribaldi, R. E., da Silva, A. R., Smiljanic, R., & Cornejo Espinoza, D. 2021, *A&A*, 650, A194, doi: [10.1051/0004-6361/202140751](https://doi.org/10.1051/0004-6361/202140751)
- Griffin, R. E. M., & Lynas-Gray, A. E. 1999, *AJ*, 117, 2998, doi: [10.1086/300878](https://doi.org/10.1086/300878)
- Gustafsson, B., Bell, R. A., Eriksson, K., & Nordlund, A. 1975, *A&A*, 42, 407
- Gustafsson, B., Edvardsson, B., Eriksson, K., et al. 2008, *A&A*, 486, 951, doi: [10.1051/0004-6361:200809724](https://doi.org/10.1051/0004-6361:200809724)
- Hansen, T. T., Holmbeck, E. M., Beers, T. C., et al. 2018, *ApJ*, 858, 92, doi: [10.3847/1538-4357/aabacc](https://doi.org/10.3847/1538-4357/aabacc)
- Harris, C. R., Millman, K. J., van der Walt, S. J., et al. 2020, *Nature*, 585, 357, doi: [10.1038/s41586-020-2649-2](https://doi.org/10.1038/s41586-020-2649-2)
- Hauschildt, P. H., Baron, E., & Allard, F. 1997, *ApJ*, 483, 390, doi: [10.1086/304233](https://doi.org/10.1086/304233)
- Hawkins, K., Jofré, P., Heiter, U., et al. 2016, *A&A*, 592, A70, doi: [10.1051/0004-6361/201628268](https://doi.org/10.1051/0004-6361/201628268)
- Heiter, U., Jofré, P., Gustafsson, B., et al. 2015, *A&A*, 582, A49, doi: [10.1051/0004-6361/201526319](https://doi.org/10.1051/0004-6361/201526319)
- Heiter, U., Lind, K., Bergemann, M., et al. 2021, *A&A*, 645, A106, doi: [10.1051/0004-6361/201936291](https://doi.org/10.1051/0004-6361/201936291)
- Holmbeck, E. M., Hansen, T. T., Beers, T. C., et al. 2020, *ApJS*, 249, 30, doi: [10.3847/1538-4365/ab9c19](https://doi.org/10.3847/1538-4365/ab9c19)
- Hubeny, I., & Mihalas, D. 2014, *Theory of Stellar Atmospheres*
- Hunter, J. D. 2007, *Computing in Science & Engineering*, 9, 90, doi: [10.1109/MCSE.2007.55](https://doi.org/10.1109/MCSE.2007.55)
- Jofré, P., Heiter, U., & Soubiran, C. 2019, *ARA&A*, 57, 571, doi: [10.1146/annurev-astro-091918-104509](https://doi.org/10.1146/annurev-astro-091918-104509)
- Jofré, P., Heiter, U., Soubiran, C., et al. 2014, *A&A*, 564, A133, doi: [10.1051/0004-6361/201322440](https://doi.org/10.1051/0004-6361/201322440)
- Karovicova, I., White, T. R., Nordlander, T., et al. 2021a, arXiv e-prints, arXiv:2109.06203. <https://arxiv.org/abs/2109.06203>
- . 2021b, arXiv e-prints, arXiv:2109.13258. <https://arxiv.org/abs/2109.13258>
- . 2020, *A&A*, 640, A25, doi: [10.1051/0004-6361/202037590](https://doi.org/10.1051/0004-6361/202037590)
- . 2018, *MNRAS*, 475, L81, doi: [10.1093/mnrasl/sly010](https://doi.org/10.1093/mnrasl/sly010)
- Kobayashi, C., Umeda, H., Nomoto, K., Tominaga, N., & Ohkubo, T. 2006, *ApJ*, 653, 1145, doi: [10.1086/508914](https://doi.org/10.1086/508914)
- Kollmeier, J. A., Zasowski, G., Rix, H.-W., et al. 2017, arXiv e-prints, arXiv:1711.03234. <https://arxiv.org/abs/1711.03234>
- Kovalev, M., Bergemann, M., Ting, Y.-S., & Rix, H.-W. 2019, *A&A*, 628, A54, doi: [10.1051/0004-6361/201935861](https://doi.org/10.1051/0004-6361/201935861)
- Lacour, S., Meimon, S., Thiébaut, E., et al. 2008, *A&A*, 485, 561, doi: [10.1051/0004-6361:200809611](https://doi.org/10.1051/0004-6361:200809611)
- Li, Y., & Ezzeddine, R. 2023, LOTUS: v0.1.1, v0.1.1, Zenodo, doi: [10.5281/zenodo.7502804](https://doi.org/10.5281/zenodo.7502804)
- Lind, K., Bergemann, M., & Asplund, M. 2012, *MNRAS*, 427, 50, doi: [10.1111/j.1365-2966.2012.21686.x](https://doi.org/10.1111/j.1365-2966.2012.21686.x)
- Linsky, J. L. 2017, *ARA&A*, 55, 159, doi: [10.1146/annurev-astro-091916-055327](https://doi.org/10.1146/annurev-astro-091916-055327)
- Liu, C., Fu, J., Shi, J., et al. 2020, arXiv e-prints, arXiv:2005.07210. <https://arxiv.org/abs/2005.07210>
- Magrini, L., Randich, S., Friel, E., et al. 2013, *A&A*, 558, A38, doi: [10.1051/0004-6361/201321844](https://doi.org/10.1051/0004-6361/201321844)
- Mashonkina, L., Gehren, T., Shi, J. R., Korn, A. J., & Grupp, F. 2011, *A&A*, 528, A87, doi: [10.1051/0004-6361/201015336](https://doi.org/10.1051/0004-6361/201015336)
- Mashonkina, L., Jablonka, P., Sitnova, T., Pakhomov, Y., & North, P. 2017, *A&A*, 608, A89, doi: [10.1051/0004-6361/201731582](https://doi.org/10.1051/0004-6361/201731582)
- McWilliam, A. 1997, *ARA&A*, 35, 503, doi: [10.1146/annurev.astro.35.1.503](https://doi.org/10.1146/annurev.astro.35.1.503)

- Metropolis, N., & Ulam, S. 1949, Journal of the American Statistical Association, 44, 335, doi: [10.1080/01621459.1949.10483310](https://doi.org/10.1080/01621459.1949.10483310)
- Meurer, A., Smith, C. P., Paprocki, M., et al. 2017, PeerJ Computer Science, 3, e103, doi: [10.7717/peerj-cs.103](https://doi.org/10.7717/peerj-cs.103)
- Miesch, M. S., & Toomre, J. 2009, Annual Review of Fluid Mechanics, 41, 317, doi: [10.1146/annurev.fluid.010908.165215](https://doi.org/10.1146/annurev.fluid.010908.165215)
- Miglio, A., Chiappini, C., Mosser, B., et al. 2017, Astronomische Nachrichten, 338, 644, doi: [10.1002/asna.201713385](https://doi.org/10.1002/asna.201713385)
- Mihalas, D., & Athay, R. G. 1973, ARA&A, 11, 187, doi: [10.1146/annurev.aa.11.090173.001155](https://doi.org/10.1146/annurev.aa.11.090173.001155)
- Morel, T., Miglio, A., Lagarde, N., et al. 2014, VizieR Online Data Catalog, J/A+A/564/A119
- Mucciarelli, A., Pancino, E., Lovisi, L., Ferraro, F. R., & Lapenna, E. 2013, ApJ, 766, 78, doi: [10.1088/0004-637X/766/2/78](https://doi.org/10.1088/0004-637X/766/2/78)
- Neal, R. M. 2003, The Annals of Statistics, 31, 705, doi: [10.1214/aos/1056562461](https://doi.org/10.1214/aos/1056562461)
- Osorio, Y., Barklem, P. S., Lind, K., et al. 2015, A&A, 579, A53, doi: [10.1051/0004-6361/201525846](https://doi.org/10.1051/0004-6361/201525846)
- pandas development team, T. 2020, pandas-dev/pandas: Pandas, latest, Zenodo, doi: [10.5281/zenodo.3509134](https://doi.org/10.5281/zenodo.3509134)
- Piskunov, N., & Valenti, J. A. 2017, A&A, 597, A16, doi: [10.1051/0004-6361/201629124](https://doi.org/10.1051/0004-6361/201629124)
- Plez, B. 2012, Turbospectrum: Code for spectral synthesis, Astrophysics Source Code Library, record ascl:1205.004. <http://ascl.net/1205.004>
- Quirrenbach, A., Mozurkewich, D., Buscher, D. F., Hummel, C. A., & Armstrong, J. T. 1996, A&A, 312, 160
- Ramírez, I., & Allende Prieto, C. 2011, ApJ, 743, 135, doi: [10.1088/0004-637X/743/2/135](https://doi.org/10.1088/0004-637X/743/2/135)
- Recio-Blanco, A., Bijaoui, A., & de Laverny, P. 2006, MNRAS, 370, 141, doi: [10.1111/j.1365-2966.2006.10455.x](https://doi.org/10.1111/j.1365-2966.2006.10455.x)
- Roederer, I. U., Sakari, C. M., Placco, V. M., et al. 2018, The Astrophysical Journal, 865, 129, doi: [10.3847/1538-4357/aadd92](https://doi.org/10.3847/1538-4357/aadd92)
- Rybicki, G. B., & Hummer, D. G. 1991, A&A, 245, 171
- Sakari, C. M., Placco, V. M., Farrell, E. M., et al. 2018, ApJ, 868, 110, doi: [10.3847/1538-4357/aae9df](https://doi.org/10.3847/1538-4357/aae9df)
- Salvatier, J., Wiecki, T. V., & Fonnesbeck, C. 2016, PeerJ Computer Science, 2, e55
- Sbordone, L., Caffau, E., Bonifacio, P., & Duffau, S. 2014, A&A, 564, A109, doi: [10.1051/0004-6361/201322430](https://doi.org/10.1051/0004-6361/201322430)
- Sousa, S. G., Santos, N. C., Adibekyan, V., Delgado-Mena, E., & Israelian, G. 2015, A&A, 577, A67, doi: [10.1051/0004-6361/201425463](https://doi.org/10.1051/0004-6361/201425463)
- Steinmetz, M., Matijević, G., Enke, H., et al. 2020, AJ, 160, 82, doi: [10.3847/1538-3881/ab9ab9](https://doi.org/10.3847/1538-3881/ab9ab9)
- Storn, R., & Price, K. 1996, in Proceedings of IEEE International Conference on Evolutionary Computation, 842–844, doi: [10.1109/ICEC.1996.542711](https://doi.org/10.1109/ICEC.1996.542711)
- Taberner, H. M., Marfil, E., Montes, D., & González Hernández, J. I. 2019, A&A, 628, A131, doi: [10.1051/0004-6361/201935465](https://doi.org/10.1051/0004-6361/201935465)
- Takeda, Y., Sato, B., Kambe, E., et al. 2005, PASJ, 57, 109, doi: [10.1093/pasj/57.1.109](https://doi.org/10.1093/pasj/57.1.109)
- Takeda, Y., & Tajitsu, A. 2015, MNRAS, 450, 397, doi: [10.1093/mnras/stv682](https://doi.org/10.1093/mnras/stv682)
- Team, T. T. D., Al-Rfou, R., Alain, G., et al. 2016, arXiv preprint arXiv:1605.02688
- Tsantaki, M., & Andreassen, D. 2021, in The 20.5th Cambridge Workshop on Cool Stars, Stellar Systems, and the Sun (CS20.5), Cambridge Workshop on Cool Stars, Stellar Systems, and the Sun, 172, doi: [10.5281/zenodo.4565462](https://doi.org/10.5281/zenodo.4565462)
- Tsantaki, M., Santos, N. C., Sousa, S. G., et al. 2019, MNRAS, 485, 2772, doi: [10.1093/mnras/stz578](https://doi.org/10.1093/mnras/stz578)
- van der Walt, S., Colbert, S. C., & Varoquaux, G. 2011, Computing in Science and Engineering, 13, 22, doi: [10.1109/MCSE.2011.37](https://doi.org/10.1109/MCSE.2011.37)
- Vanderburg, A., Plavchan, P., Johnson, J. A., et al. 2016, MNRAS, 459, 3565, doi: [10.1093/mnras/stw863](https://doi.org/10.1093/mnras/stw863)
- Virtanen, P., Gommers, R., Oliphant, T. E., et al. 2020, Nature Methods, 17, 261, doi: [10.1038/s41592-019-0686-2](https://doi.org/10.1038/s41592-019-0686-2)
- Wehrhahn, A. 2021, in The 20.5th Cambridge Workshop on Cool Stars, Stellar Systems, and the Sun (CS20.5), Cambridge Workshop on Cool Stars, Stellar Systems, and the Sun, 1, doi: [10.5281/zenodo.4537913](https://doi.org/10.5281/zenodo.4537913)
- Wijbenga, J. W., & Zwaan, C. 1972, SoPh, 23, 265, doi: [10.1007/BF00148089](https://doi.org/10.1007/BF00148089)
- Worley, C. C., Jofré, P., Rendle, B., et al. 2020, A&A, 643, A83, doi: [10.1051/0004-6361/201936726](https://doi.org/10.1051/0004-6361/201936726)

Zhao, G., Zhao, Y., Chu, Y., Jing, Y., & Deng, L.
2012, arXiv e-prints, arXiv:1206.3569.
<https://arxiv.org/abs/1206.3569>